NORTHWESTERN UNIVERSITY

Performance and Structural Evolution of Nano-Scale Infiltrated Solid Oxide Fuel Cell Cathodes

A DISSERTATION

SUBMITTED TO THE GRADUATE SCHOOL
IN PARTIAL FULFILLMENT OF THE REQUIREMENTS

for the degree

DOCTOR OF PHILOSOPHY

Field of Materials Science and Engineering

By

Ann Virginia Call

EVANSTON, ILLINOIS

March 2017

Abstract

**Performance and Structural Evolution of Nano-Scale
Infiltrated Solid Oxide Fuel Cell Cathodes**

Ann Virginia Call

Nano-structured mixed ionic and electronic conducting (MIEC) materials have garnered intense interest in electrode development for solid oxide fuel cells due to their high surface areas which allow for effective catalytic activity and low polarization resistances. In particular, composite solid oxide fuel cell (SOFC) cathodes consisting of ionic conducting scaffolds infiltrated with MIEC nanoparticles have exhibited some of the lowest reported polarization resistances. In order for cells utilizing nanostructured morphologies to be viable for commercial implementation, more information on their initial performance and long term stability is necessary. In this study, symmetric cell cathodes were prepared via wet infiltration of $Sr_{0.5}Sm_{0.5}CoO_3$ (SSC) nano-particles via a nitrate process into porous $Ce_{0.9}Gd_{0.1}O_{1.95}$ (GDC) scaffolds to be used as a model system to investigate performance and structural evolution. Detailed analysis of the cells and cathodes was carried out using electrochemical impedance spectroscopy (EIS). Initial polarization resistances (R_P) as low as 0.11 Ω cm^2 at 600ºC were obtained for these SSC-GDC cathodes, making them an ideal candidate for studying high performance nano-structured electrodes.

The present results show that the infiltrated cathode microstructure has a direct impact on the initial performance of the cell. Small initial particle sizes and high infiltration loadings (up to

30 vol% SSC) improved initial R_P. A simple microstructure-based electrochemical model successfully explained these trends in R_P. Further understanding of electrode performance was gleaned from fitting EIS data gathered under varying temperatures and oxygen partial pressures to equivalent circuit models. Both RQ and Gerischer impedance elements provided good fits to the main response in the EIS data, which was associated with the combination of oxygen surface exchange and oxygen diffusion in the electrode. A gas diffusion response was also observed at relatively low pO_2.

The cells were subjected to life testing at temperatures between 650°C and 800°C for as long as 1500 h. EIS measurements, carried out periodically during the life tests, were done in air at 600°C, a typical expected intermediate-temperature SOFC operating temperature. These were accelerated tests because the aging temperatures > 600°C should accelerate most degradation processes such as nano-particle coarsening. Long-term R_P versus time data was fitted to a combined surface resistance and coarsening kinetics model, and a $t^{0.25}$ power law coarsening model was found to provide the best fits to the data, suggesting that surface diffusion is the dominant mass transport pathway in SSC-GDC infiltrated cathodes. That is, cathode degradation was due primarily to the coarsening-induced decrease in active SSC surface area. Scanning electron microscopy (SEM) performed after electrochemical life testing confirmed the extent of coarsening of the SSC nanoparticles. The model is used to make predictions regarding long-term stability of infiltrated SSC electrodes, and is also compared with prior results on a similar perovskite MIEC electrode, LSCF. An important new finding is that increasing infiltration loadings yields a marked decrease in the long term degradation rate. Predictions based on accelerated life tests found the

lowest possible operating temperature while achieving a degradation rate of 0.5% per kh is 595°C, corresponding to an initial particle size of 40 nm.

Acknowledgements

First and foremost, I would like to thank my advisor Prof. Scott Barnett. Without your guidance and support, this work would not have been possible. When my experiments did not work the way we expected and the analysis got hairy, you were supportive and made me feel optimistic about my "interesting" findings.

Secondly I would like to express my gratitude to my committee: Prof. Peter Voorhees, Prof. Thomas Mason, and Prof. Jason Nicholas; for guiding me through this journey. In particular, Prof. Jason Nicholas for his support in training me in many of the techniques used in this dissertation and for taking the time at the beginning of my time at NU to help me transition into graduate work.

Prof. Ellen Ivers-Tiffée from the Karlsruhe Institute of Technology in Karlsruhe, Germany was incredibly accommodating by allowing me to visit her laboratory for four months in 2012. She and her entire group made me feel welcome during my stay there. In particular, Dr. Jan Hayd, Jochen Joos, Dr. Dino Klotz, Helge Geisler, and Michael Schönleber for not only assisting in my research, but also for helping me explore Karlsruhe and not laughing too hard at my attempts at speaking German.

The entire Barnett Research Group, past and present: all of you are an inspiration, not only for my work, but for many of the ridiculous hijinks that I've gotten myself into over the past five years. I'll miss organizing all of our seasonal group events (which always land in the wrong season).

Dr. Justin Railsback in particular needs to be thanked for his contribution in furthering the

analysis of the long term degradation work and his diligence in working to get the data published.

The entire Materials Science and Engineering PhD class needs to be thanked for keeping me sane. I don't think I would have survived if we weren't such a tight knit community.

Stephen Harm and all of the Warehouse staff back in WI, I probably wouldn't have grown up to be the person that I am today without all of you. It's strange to think that a tiny concert venue in the middle of nowhere raised me, but there you have it. All of you have been the family and friends that I've needed. You all taught me to not only dream big, but to put in the work to make it happen.

To my sister Sarah Jacobson, for being the one consistent source of encouragement in my life: thank you for always telling me to do what I want. Without you there to tell me to follow my dreams and think about myself, I probably would have listened to Mom and Chin and not gone to college. All of this work is definitely your fault, and I can never thank you enough.

Table of Contents

List of Figures

Chapter 1

Introduction

Solid Oxide Fuel Cells (SOFCs) are one of a class of energy conversion devices which uses an oxidant and a fuel to convert chemical energy to electrical energy. Although SOFCs can reach efficiencies of over 60%, more than twice that of an internal combustion engine [1-5], they are not currently in widespread commercial use. This is because fuel cell performance is currently limited by the materials utilized in its construction. By lowering the operating temperature, more cost-effective materials can be used for system components and a wider range of materials can be utilized in cell development [2, 4, 6-9]. However, the resistance of the electrodes and electrolyte of the fuel cell increase rapidly with decreasing temperature, causing the performance of the fuel cell to be reduced accordingly [10-13]. In low temperature operation (600°C or lower), the primary source of loss is considered to be the cathode, the electrode at which reduction occurs [2, 7, 13]. A large focus in current SOFC research is on improving electrode microstructures and materials to lower the operating temperature with minimal losses.

One method of reducing losses originating in the cathode is to utilize nano-structured materials. There are a number of benefits to this approach, the most obvious being that reducing the average particle size of these electrocatalytic materials significantly increases the active surface area that is available for the oxygen reduction reaction to occur, resulting in low area specific polarization resistance (R_P). Additionally, the multiple step processing that is used to produce composite nano-structured materials allows for separate formation temperatures for the different components and opens the possibility of using materials which cannot otherwise be used due to

incompatible reactivity during high temperature formation and co-sintering temperatures between cell components.

The most common cathode materials in use today are perovskites which exhibit high surface activity for the oxygen reduction reaction at intermediate operating temperatures. Typical materials that are of interest for intermediate temperature operation are $La_{1-x}Sr_xMnO_{3-\delta}$ (LSM), $La_{1-x}Sr_xCo_{1-y}Fe_yO_{3-\delta}$ (LSCF), $Sm_{0.5}Sr_{0.5}CoO_{3-\delta}$ (SSC), $Ba_{0.5}Sr_{0.5}Co_{0.8}Fe_{0.2}O_{3-\delta}$ (BSCF), and $LaNi_{1-x}Fe_xO_{3-\delta}$ (LNF) [6, 14]. Of these materials, SSC was chosen as the model system for a number of reasons: it has been previously characterized for its bulk properties in the literature [6, 9, 11, 15], it has very low reported values of R_P – SSC nano-composite cathodes have reported R_P literature values as low as 0.21 Ω cm^2 at 500°C and 0.052 Ω cm^2 at 600°C [16], it is chemically compatible with other cell components in our system ($Ce_{0.9}Gd_{0.1}O_{1.95}$ (GDC), LSM, Ag), and it is relatively simple to produce phase-pure nano-material via nitrate decomposition [17, 18].

Although the perovskite cathode materials have been characterized for their bulk material properties, it is still important to understand the underlying rate-limiting behavior of these materials under electrochemical operation. This is particularly true for nano-structured materials, as we are most interested in the proportional change in observed surface activity for the oxygen reduction reaction with increasing active surface area and how microstructure modification affects cell performance, but also because the intrinsic properties of the materials could change with significant changes in size. A complete understanding of electrochemical loss mechanisms is necessary in order to improve performance through rational design.

A significant drawback to nano-structured electrodes is their unknown long-term stability

at operating temperature (~500-700°C). The combination of elevated operating temperature and high interfacial area of the nanostructure can drive coarsening behavior and increase degradation rates. In order for nano-scale materials to be commercially feasible, performance stability will need to meet or beat degradation requirements related to the U.S. Department of Energy 2015 target for stationary power, 0.5% per kh, and next the more stringent 2020 target of 0.2% per kh over the expected SOFC operation lifetime of 40,000 h [19-21]. At the laboratory scale it is not feasible to conduct 40,000 h life tests, so it is necessary to develop accelerated degradation testing techniques and models.

The objective of this dissertation is to explore a state-of-the-art MIEC perovskite electrode material, SSC, infiltrated into GDC scaffolds, in order to advance the understanding of the electrochemical processes and long term performance of nano-scale infiltrated cathodes. Cathodes tested were prepared in symmetric GDC-electrolyte cells via wet infiltration of SSC nano-particles via a nitrate process into porous GDC scaffolds.

Chapter 2

Background

2.1   Solid Oxide Fuel Cells

Solid oxide fuel cells (SOFCs) are solid state devices, which convert chemical energy into electrical energy and heat. Fuel is oxidized at the anode while oxygen is reduced at the cathode. The electrolyte acts as both an oxygen ion conductor and an electrical barrier which forces the electrons through an external circuit, producing useful work in the form of DC electricity. Oxygen ions travel through the electrolyte due to a potential gradient in the system which develops in response to half-cell reactions occurring at both the anode and the cathode, as is described by the Nernst Potential, E, which relates the reversible cell voltage, E^0, as a function of chemical activity [2, 4]:

$$(2.1) \qquad E = E^0 - \frac{R\,T}{n\,F} \ln \frac{\Pi\, a_{products}^{v_i}}{\Pi\, a_{reactants}^{v_i}}$$

Where $a_{products}^{v_i}$ and $a_{reactants}^{v_i}$ are the activities of products and reactants, respectively. Electrons and oxygen ions then reunite at the anode to react with a fuel, such as hydrogen, to produce heat. A schematic which includes the chemical half reactions occurring at each electrode during hydrogen-oxygen use is shown in Figure 2.1. The inherent potential difference between the anode and cathode in the fuel cell system is due to the presence and separation of fuels and oxidants, which ensures that electricity and heat will be generated as long as these reactants and an available

electrical pathway between these two components are available [2, 4].
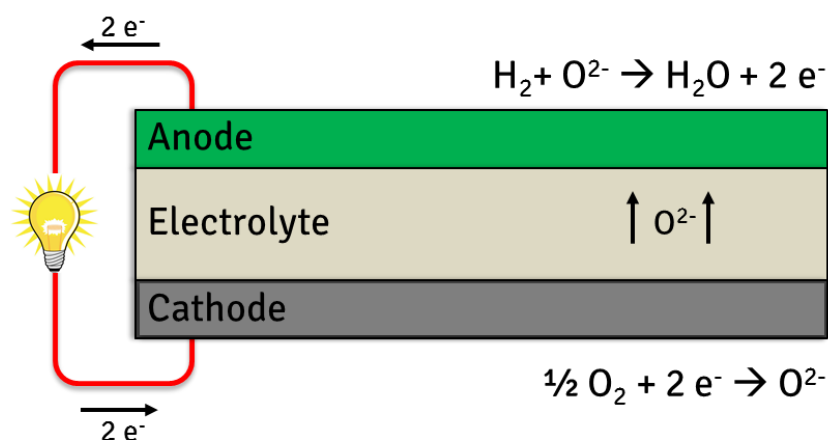
Figure 2.1: Schematic of a SOFC consisting of a porous anode and porous cathode separated by a dense electrolyte. Oxygen is reduced at the cathode and the oxygen ions are transported through the electrolyte and electrons flow through an external circuit to produce useful work before recombining with at the anode to react with hydrogen to produce water.

Although there are several types of fuel cells [2], SOFCs are a particularly promising energy conversion device due to the inherent properties of the system. SOFCs exhibit high power densities in comparison to other fuel cell systems, fuel flexibility, and high efficiencies of up to 60% [1-5, 20]. Additionally, the waste heat produced can be utilized in a number of residential and industrial uses such as water heating or reducing the cost of high temperature processes, thereby increasing efficiencies further [1, 2, 4].

The primary components of a SOFC are the electrolyte, cathode, anode, and interconnect. Each of these components has their own materials and engineering requirements. The scope of the present work will focus on the cathode, which is discussed in further detail in the pages following.

2.2   Cathodes

The reduction of oxygen occurs at the cathode, with a high-performance cathode exhibiting

the following traits [2, 6, 7]:

- Catalytically active toward the reduction of oxygen

- Electronically and ionically conductive to allow for sufficient transport to the external circuit and the electrolyte respectively

- Sufficiently porous to allow the flow of oxidant to active sites in the electrode

- Chemically and mechanically compatible with the electrolyte and interconnect under operating conditions, and with temperature and/or current cycling

As the operating temperature is decreased the number of materials which meet these

conditions increases, allowing for a wider range of low cost materials to be used. A consequence

of decreased temperature is decreased conductivity and catalytic activity of cathode materials. At

low and intermediate operating temperatures, 700°C and below, the cathode is considered the main

source of loss in SOFCs. Cathode materials exhibit slow oxygen-reduction and ion transport

kinetics at these temperatures, which lead to high polarization resistances (R_P) and performance

loss [4, 6, 14].

For the oxygen-reduction reaction to take place, it must occur at a site which is catalytically

active, has sufficient access to gas phase reactant (oxygen), and is both electronically and ionically

conductive to allow for electrons to flow through an external circuit and ions to jump to the

electrolyte. In order to effectively increase performance, research into both cathode materials and

cathode microstructures is necessary.

Currently, the most common electrode material is $La_{1-x}Sr_xMnO_{3-\delta}$ (LSM) mixed with 8% yttria-stabilized zirconia (YSZ) to form a two-phase composite cathode [6, 14]. A representation of a traditional composite cathode microstructure is shown in Figure 2.2. The low ionic conductivity of LSM requires that it be mixed with a strong ionic conductor to increase performance. The primary advantage of two-phase cathodes is that the properties of both the ionic conducting phase and the electronic conducting phase can be optimized separately. This not only allows for easier materials selection depending on operating conditions, but also can increase the overall performance of the cathode in comparison to single-phase electrodes.
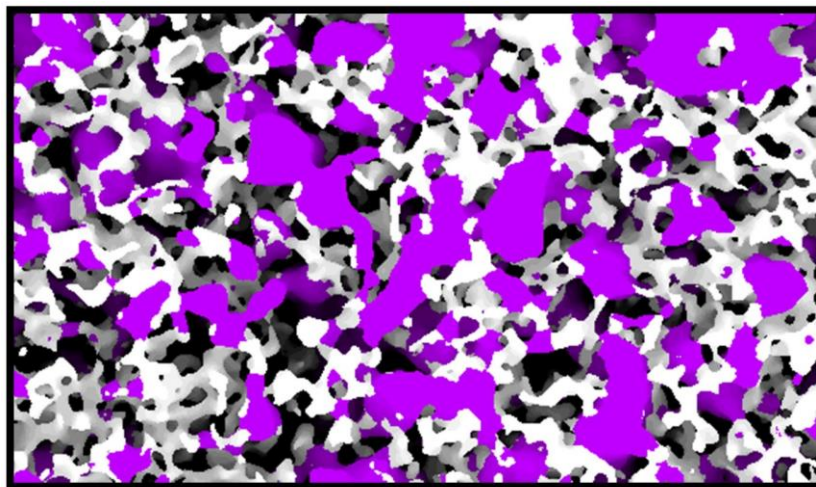
Figure 2.2: Three-dimensional representation of traditionally prepared ceramic composite electrode microstructure. The electrically conducting material, typically LSM, is represented in purple and the ionically conducting material, typically YSZ, is represented by white. Open porosity is represented by black.

There are a number of ways to incorporate multiple phases. The most common method is to simply mix the materials in powder form together and co-deposit them via screen-printing or

tape casting, as is done with LSM-YSZ cathodes [22]. Another method that is of particular interest for this project is infiltrated cathodes, which will be discussed in further detail in the following section.

2.2.1   Infiltrated Cathodes

A number of groups have reported promising reduced-temperature performance using cathodes that are comprised of nano-scale mixed ionic and electronic conducting (MIEC) materials [6, 12, 17, 23-28]. MIEC materials are active for the oxygen reduction reaction over their free surfaces, while the nano-scale structure provides a high surface area.

Infiltrated cathode microstructures are typically comprised of either ionically conducting or electronically conducting scaffolds paired with electronically or ionically conducting nano-particles respectively [6, 12, 14]. Research efforts have been made in both configurations, with advantages and disadvantages being apparent in both systems. Electronic scaffold configurations tend to allow for easy formation of the desired nano-particle infiltrate phase, but require high infiltrate volume percent to achieve good performance - limiting pore volume within the cathode. Ionic scaffold configurations require fewer infiltration steps, however infiltration of the desired composition is more difficult [6, 29]. The present work will focus on the latter.

Regardless of which material acts as the scaffold or the infiltrate, the resulting microstructure of the cathode plays a key role in the performance of the cell. Reports in the literature give varying values for R_P vs. infiltration loading, and performance is more often attributed to the fine microstructure of the cathode layer than to the relative amount of active

material. It is most often seen that cathodes with high surface areas, both scaffold and infiltrate material, and high loading result in very low, and often record-breaking, values for R_P at $t = 0$ [30]. This is often achieved by infiltrating the scaffold material many times, resulting in increasing surface area coverage. A computer generated representation of this process is shown in Figure 2.3.
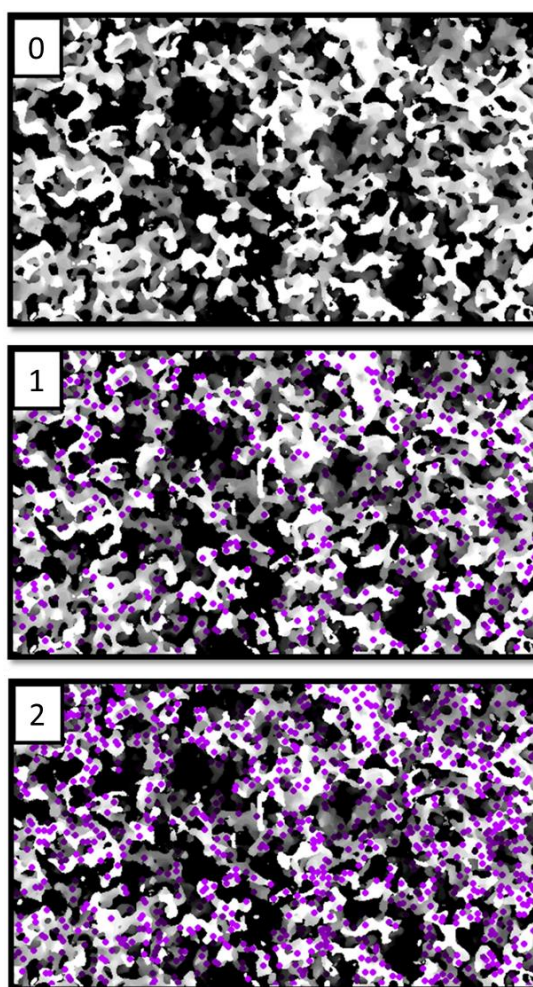
Figure 2.3: Three- dimensional representation of an infiltrated cathode (computer generated). Scaffold is represented in white, infiltrated particles are represented in purple, and pore is represented by black. 0) scaffold with zero infiltrations, 1) scaffold after one infiltration, 2) scaffold after two infiltrations.

While the initial performance of infiltrated cathodes is promising, the long term stability

of nano-scale materials under SOFC operating conditions has not been extensively investigated.

At elevated temperatures for long periods of time, the infiltrated nanoparticles in these cathodes

may coarsen significantly, leading to reduced active areas and a decrease in performance [31-36].

Extended testing of several materials systems is unrealistic at the laboratory stage due to the long

expected lifetimes (t > 40,000 h) [20, 21] of these devices as well as the near limitless number of

unique system parameters to be investigated. This places a premium on mechanistic modeling of

degradation and electrochemical mechanisms, which can be used to predict long-term behavior

based on a number of shorter, accelerated tests.

2.3   Performance and Evaluation

The ever-increasing number of potential cathode materials and long testing times make

modeling techniques for accurately determining cathode performance necessary to identify and

develop materials that provide the requisite performance and stability. Computational attempts

have been made to understand the reaction kinetics involved [37-39]; however the complexity of

cathode materials and microstructures causes difficulty in accurately modeling a wide variety of

material systems in varied operating conditions. In order for infiltrated cathodes to be a viable

choice, both initial performance and long term behavior must be characterized.

2.3.1   Initial Microstructure and Performance

Microstructure-based models have been proposed to predict the initial performance of

mixed conducting materials, most notably the Tanner-Fung-Virkar (TFV) [39] and Simple Infiltrated Microstructure Polarization Loss Estimation (SIMPLE) models [17, 23, 40]. Good agreement with experimental results for these models makes apparent that the model assumptions - material properties, microstructure, and transport kinetics play a significant role in cathode performance - must be valid.

Initial microstructure and performance of infiltrated cathodes will be covered in Chapters 2, 3, and 4. Chapter 2 will cover studies in determining if the concentration and number of high temperature infiltration steps has a significant impact on initial infiltrate particle sizes. Fractured cathodes are studied via SEM image analysis to determine if the particle size achieved during infiltration can be tuned.

Previous work has shown that the SIMPLE model is a sufficiently accurate predictor of R_P values for LSCF nano-infiltrated cathodes [17]. This is true in systems where contributions from gas-phase diffusion, the ionic conductor-MIEC interface reactions, electronic transport losses in the MIEC, or ionic transport losses in the MIEC are negligible [17, 39, 40]. Results from this study are presented in Chapter 3 of this dissertation.

Finally, Chapter 4 covers an in-depth study of the effect of varying partial pressures of oxygen and temperature on LSCF-GDC infiltrated symmetric cells. In cooperation with the Ivers-Tiffée group at Karlsruhe Institute of Technology, advanced EIS tests were completed to verify the transport properties of novel infiltrated cathodes. Symmetric cell cathodes of varying infiltrate amounts and varying oxygen partial pressures were tested to obtain a clearer understanding of the reaction mechanisms occurring within these novel cathodes and how it relates to the overall

performance of these cells.

2.3.2   Long Term Performance and Degradation

Although the R_P of cathode materials at t = 0 is important to assessing the expected performance of cathode materials, considerable work needs to be completed in order to predict how these materials will evolve over time. Evolution at these time scales is difficult to realize due to lack of long term data on these systems, as well as the inherent complexity of fuel cell systems themselves.

Annealing can be used to accelerate coarsening degradation effects and to predict R_P at long time scales. Infiltrated SSC-GDC symmetric cell cathodes were assessed for their long term performance capabilities using this method. Accelerated degradation tests were completed on SSC-GDC symmetric cell cathodes following the experimental design of Shah [34, 35]; with the added change of infiltrate percentage. An improved model for predicting long term performance from these degradation tests is discussed in Chapter 3 and the results from this study are shown in Chapter 6.

2.4   Summary and Conclusions

Solid Oxide Fuel Cells (SOFCs) are promising energy conversion devices that deliver high efficiencies, high power densities, and are fuel flexible. A major road block for widespread commercialization is performance limitations by the materials utilized in construction. In low temperature operation (600°C or lower), the primary source of loss is considered to be the cathode

and subsequently a large focus in current SOFC research is on improving cathode microstructures and materials to improve performance.

Groups studying the performance of infiltrate cathodes have reported some of the lowest values of R_P for cathode materials. While the initial performance of infiltrated cathodes is promising, the long term stability of these nano-scale materials under SOFC operating conditions has not been extensively investigated. The focus of this dissertation is to use known material parameters to aid in predicting both the initial performance of infiltrated cathodes and their long term degradation behavior.

Chapter 3

Methods

The work detailed in this thesis necessitated a very rigorous procedure in producing, testing, and analyzing the resulting data. As is seen in the literature [6, 17, 23, 35, 36] and most notably in Chapters 4 and 7 of this thesis, microstructure plays a significant role in determining the polarization resistance (R_P) of an infiltrated cathode and the conditions which SOC devices are operated, specifically the temperature in the case of nano-infiltrated cathodes, facilitate microstructure evolution resulting in degradation. Control over both the initial microstructure and the methodology used in accelerated degradation studies is necessary in order to track the results to our proposed models. To this end, Section 3.1 covers cell fabrication and Section 3.2 details the testing equipment and accelerated coarsening procedures used in this thesis. Details on the derivation of the equations used to model cell behavior and predict cathode degradation due to coarsening are outlined in Section 3.3 to both appropriately compare and contrast the appropriateness of the results obtained using such models and also to not detract from the results and discussion in later Chapters. Finally, the method used to verify nano-particle coarsening in the symmetric cells tested are discussed in Section 3.4.

3.1   Cell Fabrication

Symmetric cell cathodes were used in this study consisting of porous $Ce_{0.9}Gd_{0.1}O_{1.95}$ (GDC) scaffolds that are coated with either $Sr_{0.5}Sm_{0.5}CoO_{3-\delta}$ (SSC) or $La_{0.6}Sr_{0.4}Co_{0.2}Fe_{0.8}O_{3-\delta}$ (LSCF) nanoparticles, which act as the active electrode. Separating the two infiltrated electrodes is a dense

GDC electrolyte. Both electrodes have $La_{0.85}Sr_{0.15}MnO_{3-\delta}$ (LSM) layers that act as a current collector and a silver mesh which both aids in current collection and attaches to wires used for testing the cell. It should be noted that LSM is capable of acting as a cathode material, however the thickness of the active cathode layer used is sufficiently thick,~ 25 μm, that it is electrochemically inactive and acts solely as an electronic conductor [17]. A schematic of the cell configuration can be seen in Figure 3.1. Further details on the methods used to fabricate these cells are detailed in the subsections following.
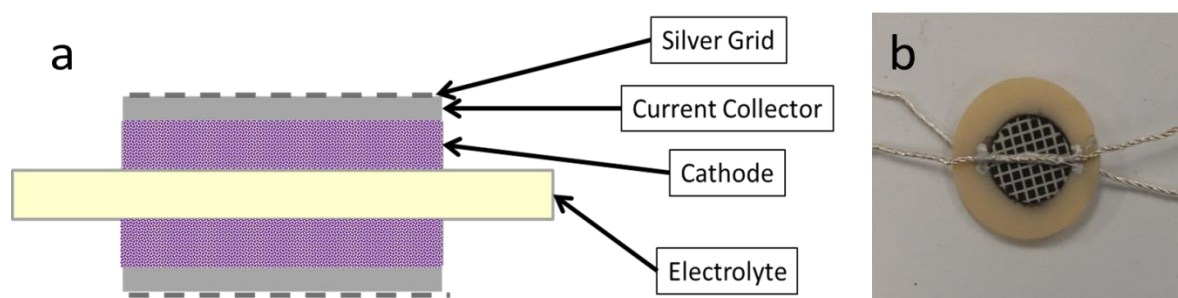
Figure 3.1: a) Schematic of a symmetric cell (not to scale), b) photo of a button cell. Electrolytes are composed of $Ce_{0.9}Gd_{0.1}O_{1.95}$ (GDC), cathodes are a GDC scaffold infiltrated with $Sr_{0.5}Sm_{0.5}CoO_{3-\delta}$ (SSC) nanoparticles, and the current collect is a $La_{0.85}Sr_{0.15}MnO_{3-\delta}$ (LSM) layer. A Ag mesh is also screen printed prior to attaching Ag wires to use as test leads.

3.1.1 Electrolyte

GDC was used as the electrolyte over the course of this work. It was selected because of its high ionic conductivity at intermediate temperatures, chemical stability in relation to the other components in the system, and also to keep consistent with previous work done on this project by Shah on LSCF-GDC infiltrated cathodes [34]. 0.5 g of GDC (Rhodia) powder was uniaxially

pressed using a ¾" inch diameter die and fired between two dense GDC weights at 600°C for 1 h to ensure burnout of any trace organics that may be present in the powder, and then ramped to 1450ºC for 6 h to achieve densification. Samples were then polished flat using 600 grit SiC sandpaper to ensure a consistently thick scaffold is screen printed on all samples.

3.1.2 Scaffold

Scaffolds of a high ionic conductivity were used in this study to complement the properties of the infiltrated nano-structure. To ensure compatibility (chemical, thermal expansion, etc.) and a reduction of charge transfer losses between the electrolyte and the scaffold, both were made from the same Rhodia GDC powder. To achieve this, a GDC ink was prepared to be used in screen printing by first coarsening Rhodia GDC powder at 800°C for 4 h. The resulting powder was mixed with an organic vehicle (Heraeus V-737) using a three-roll mill to achieve an ink with uniform distribution of GDC. 0.5 cm^2 scaffold layers were applied to both sides of the dense electrolyte by screen printing, and then fired at 600°C for 1 h to burn out the organic vehicle before ramping to 1100°C for 4 h, resulting in a cathode of ~ 25 μm thickness.

3.1.3 Infiltration

SSC precursor solution was produced by mixing the appropriate stoichiometric ratios of $Sm(NO_3)_3$, $Sr(NO_3)_2$, and $Co(NO_3)_2$ and diluting with 18.2 MΩ (Millipore) H_2O to reach a concentration of either 0.5 M or 2 M. A 2:1 ratio of citric acid-to-cation metal ions was used as a chelating agent to avoid phase separation of metals prior to nanoparticle synthesis. In the case of

using a GDC scaffold material, an additional surfactant was not necessary to aid in infiltration.

Prior to sol-gel infiltration, a mask was applied to ensure that the infiltration material was localized to only the porous GDC scaffold and not to the surrounding dense electrolyte area. Early samples utilized a water-diluted acrylic paint (Liquitex), which was carefully applied to the surrounding dense electrolyte without touching the porous scaffold layer. This method was abandoned due to the high possibility that the mask would accidentally spread into the active cathode layer during infiltration and block porosity. Later samples used a scotch-tape mask that was punched to the same size as the scaffold in order to leave the scaffold layer exposed after application. This layer could then either be removed prior to the firing step where the sol-gel was decomposed, or be decomposed along with the nitrate solution in cases where the cell was too fragile to risk peeling off the tape.

Sol-gel infiltration was completed by pipetting SSC nitrate solution onto porous GDC scaffolds. The capillary effect pulls the infiltration solution into the pore structure. Once the solution has fully receded into the scaffold, the infiltration solution was gelled at 60ºC for a minimum of 30 minutes before being decomposed in air at 800ºC for 1 h. This infiltration procedure was repeated as many times as necessary in order to achieve the infiltration loading desired. For the final infiltration step, the decomposition time is increased to 2 h to ensure phase purity of SSC. Infiltration loading was calculated using the known density of SSC and the weight change of the cell from before the start of infiltration until after the last decomposition cycle.

3.1.3.1 Monolithic Deformation

Phase purity of the resulting infiltration solutions was tested via X-ray powder diffraction (XRD) by drying the nitrate solution onto a ceramic plate and decomposing the nitrate solution at 800°C for 2 h. This corresponded to the amount of time which the infiltration solution was processed in the final infiltration step. The resulting powder was scraped off the plate and analyzed via X-ray powder diffraction using a Scintag XDS200 diffractometer at room temperature. Figure 3.2 shows the resulting X-ray spectra.
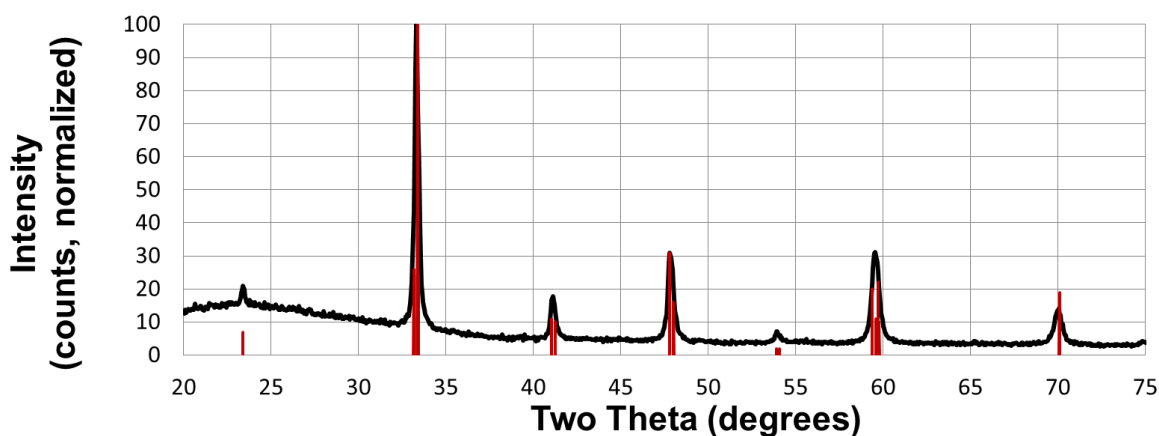
Figure 3.2:: X-ray powder diffraction pattern for SSC powder produced via sol-gel method (black) and compared to reported XRD values (red) (JCPDS card 00-053-0112).

3.1.4 Infiltration

Once the target infiltration loading was achieved, a porous LSM layer was screen printed on top of the active cathode layer to act as a current collector and fired at 600°C to burn out the organic screen printing vehicle before being ramped to 800°C for 1 h. Finally, a Ag mesh was screen printed (Heraeus-C4400UF Silver Conductor Paste) on top of the LSM current collector

and Ag leads attached for use in testing. Ag contacts were fired in-situ during ramping of the cell to operating temperatures. Firing profiles for all cell components can be found in Figure 3.3.
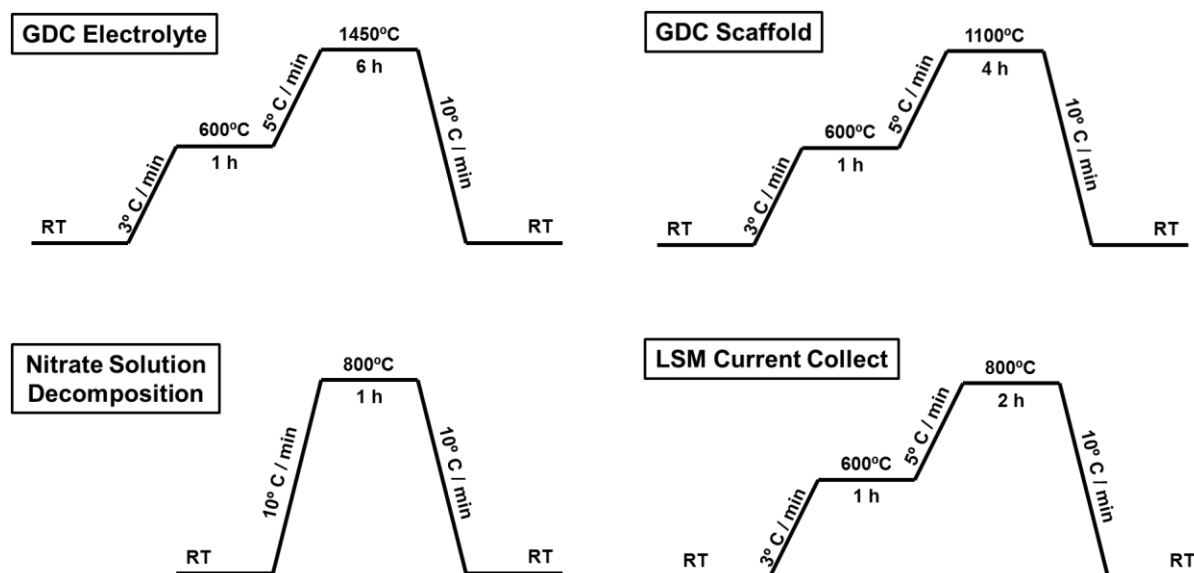
Figure 3.3: Firing profiles for each fabrication step for infiltrated symmetric cell cathodes.

3.2   EIS Testing

A determination of the polarization losses in nano-structured symmetric cell cathodes was completed using electrochemical impedance spectroscopy (EIS). This is a standard method of evaluating the performance of a SOC in the field [2, 4]. Changes in the size, shape, and characteristic frequency of the resulting impedance arcs can give significant insight into the magnitude and source of polarization resistance (R_P). Further information on the testing setup and

subsequent analysis techniques used are described in the sections following.

3.2.1   Testing Rig

Cells produced for this dissertation work were tested either at Northwestern University (Chapters 3, 6, and 7) or at the Karlsruhe Institute of Technology (KIT) (Chapter 5). Due to the very different testing setups and testing methodologies used for each, cells tested at either facility were not directly quantitatively compared to one another. Most notable of these differences were gas compositions and flow rates (stagnant air vs. flowing O_2/Ar mixtures) which may show subtle changes in mass transport which are difficult to account for accurately in the data.

3.2.1.1   Northwestern University Test Setup

A majority of the cells analyzed during the course of this dissertation were electrochemically tested at Northwestern University (NU). With the exception of the data presented in Chapter 5, all data presented in this dissertation were collected at NU. Cells were mounted on a ceramic tube and tested in a clamshell tube-furnace under stagnant ambient air. In some cases, up to four cells were tested in the same furnace, as can be seen in Figure 3.4. For these tests, all cells were placed close together and within the hot-zone of the furnace. Temperature was verified by additional K-type thermocouples, ensuring that the temperature difference experienced between cells was less than 10°C, resulting in at most a 1.6% error due to temperature variation between cells. EIS was completed using a BAS-Zahner IM6 impedance analyzer between 10-1 and 106 Hz with a 20mV amplitude AC signal and no applied DC bias.

3.2.1.2   Karlsruhe Institute of Technology Test Setup

Symmetric cell cathodes tested at KIT were used to analyze the impedance response of cells tested under varying temperature and partial pressures of oxygen. This testing setup was used in lieu of the one at NU, as it was optimized to have very low inductance contributions, which skew data at high frequencies and make circuit fitting analysis difficult. Cells were mounted in a pressure Au contact rig [40] and were tested under flowing O_2, gas balanced with Ar gas, at O_2 fractions from 1-100% at 1 atm. EIS measurements were carried out using a Solartron 1260 frequency response analyzer at frequencies between 10-1 and 106 Hz with no applied DC bias.
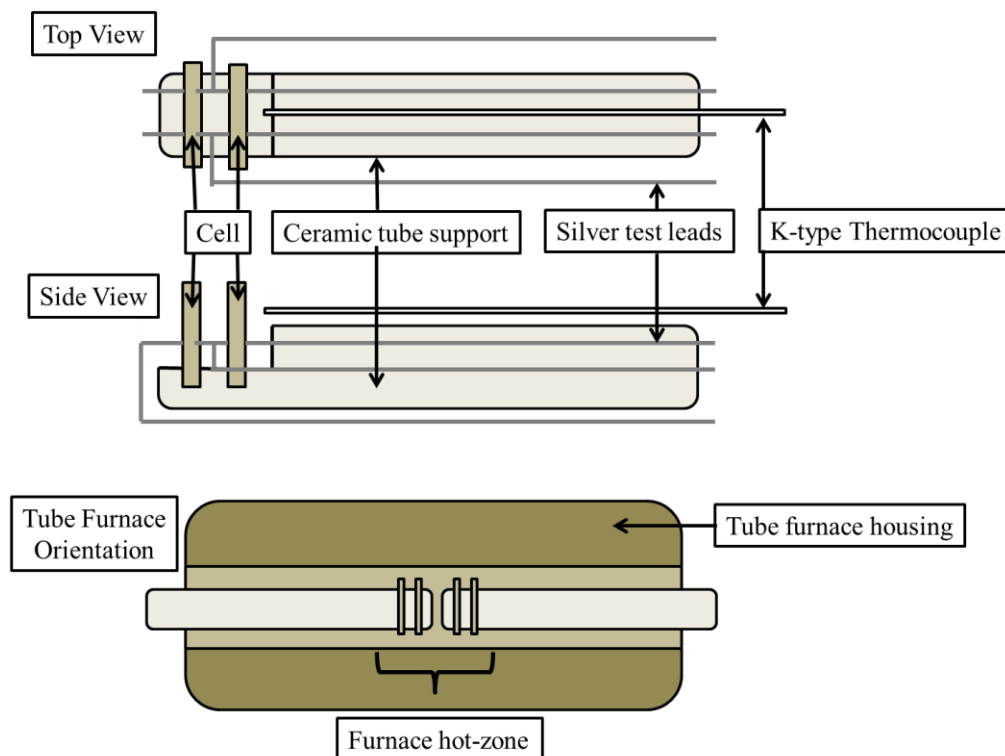
Figure 3.4: Schematic of the symmetric cell cathode testing setup used at Northwestern University. Up to four symmetric cells can be tested in the same clamshell tube-furnace.

3.3   Analysis Methods

The resulting EIS data were analyzed by measuring R_P, comparing R_P to predictions calculated using the Simple Infiltrated Microstructure Polarization Loss Estimation (SIMPLE) model, circuit fitting, analysis of differences in impedance spectra (ADIS), and calculated degradation rates using a combined surface resistance and coarsening theory model. These methods are detailed in the sections following.

3.3.1 R_P Measurement

R_P is measured to be the difference between the real intercepts of an EIS spectrum when plotted as -Imaginary Z (Z") vs. Real Z (Z') in so-called "Nyquist" fashion. This measurement is then normalized to the footprint area of the cathode, and in the case of symmetric cathodes, divided by two to account for the two electrodes being measured. The resistance associated with the value of the first intercept is the ohmic resistance, R_Ω, and the sum of R_P and R_Ω gives the total resistance associated with the cell. Figure 3.5 illustrates this.
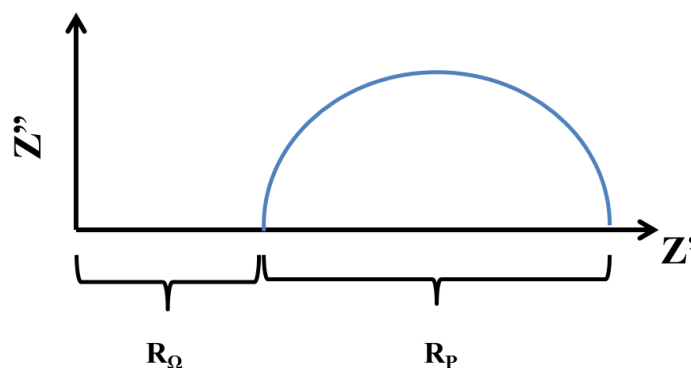
Figure 3.5: Representative Nyquist plot of fuel cell EIS data. The resistance associated with R_Ω is measured by the distance between the origin and the first intercept of on the real axis. R_P is represented by the difference between the two intercepts of the impedance curve.

3.3.2 Simple Infiltrated Microstructure Polarization Loss Estimation (SIMPLE)

Predictions for polarization resistance (R_P) were made using the Simple Infiltrated Microstructure Polarization Loss Estimation (SIMPLE) model [17, 40]. Unlike basic surface resistance calculations based on infiltrate surface area, this model accounts for losses associated with MIEC surface resistance and oxygen ion transport through the ionic-conducting scaffold material. The model is derived from the Tanner-Fung-Virkar (TFV) model [39], which was originally developed for micro-composite electrodes.
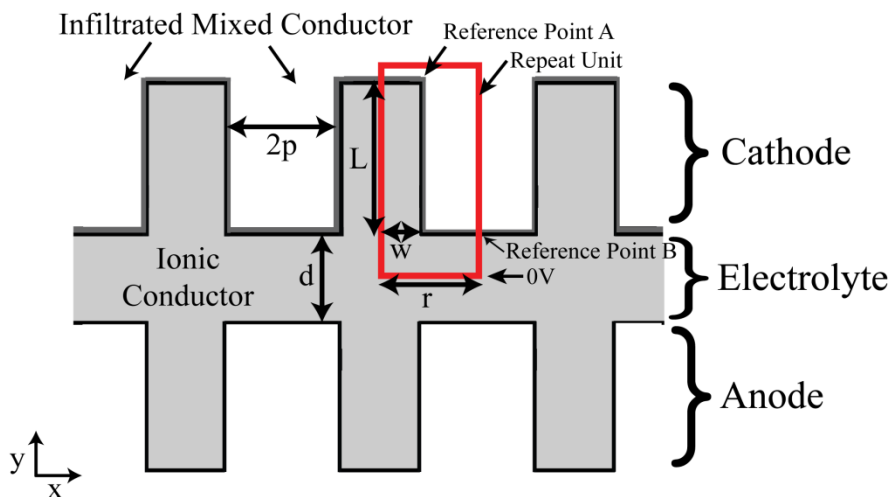
Figure 3.6: SIMPLE model idealized electrode geometry. Here the ionic conducting scaffold has been approximated as a series of columns and the infiltrated nano-particles have been approximated as an infinitely thin layer with an effective surface resistance dependent on the infiltrate surface area and the intrinsic infiltrate surface resistance, as described by Equation 3.1. Image taken from [17] with permission.

The simplified model cathode structure used in this approach can be seen in Figure 3.6. The columned simplification of the microstructure allows for the consideration of oxygen ion diffusion losses. The resistance associated with infiltrated MIEC is also simplified as a uniformly spread layer across the surface of the cathode. The resulting equations for the SIMPLE model are as follows:

$$(3.1) \qquad R_P = \frac{r\left(\frac{R_S A_{Sc}}{A_{Inf}}\right)}{\left(\frac{1+\beta}{1+\beta\,\exp\left(\frac{-2h}{\alpha}\right)}\right)r(1-p)\exp\left(\frac{-h}{\alpha}\right) + \frac{\left(1+\beta\left(\frac{-h}{\alpha}\right)\right)}{\left(1+\beta\left(\frac{-2h}{\alpha}\right)\right)}\alpha\left(1-\exp\left(\frac{-h}{\alpha}\right)\right) + pr}$$

Where

$$(3.2) \qquad \alpha = \sqrt{\sigma V_{O,Sc}^{\bullet\bullet} r(1-p)\frac{R_S A_{Sc}}{A_{Inf}}}$$

And

$$(3.3) \qquad \beta = \frac{\sigma V_{O,Sc}^{\bullet\bullet}\frac{R_S A_{Sc}}{A_{Inf}} - \alpha}{\sigma V_{O,Sc}^{\bullet\bullet}\frac{R_S A_{Sc}}{A_{Inf}} + \alpha}$$

In these equations, R_S is the surface resistance value for the infiltrate material, A_{Sc} and A_{Inf} are the surface areas associated with the scaffold and the infiltrate material respectively, and $\sigma V_{O,Sc}^{\bullet\bullet}$ refers to the ionic conductivity of the scaffold material. It is important to note that all parameters associated with this model can be determined experimentally and do not require additional fitting parameters.

This model has been shown to be a significant improvement over simple estimations of the active surface area the infiltrated material using the surface resistance model,

$$(3.4) \qquad Rp = \frac{Rs_{Inf}}{A_{Inf}/A_{FP}}$$

where the polarization resistance is equal to the surface resistance of the infiltrated material, divided by the surface area of infiltrated material normalized by the cathode footprint area, as the SIMPLE model takes into account losses associated with ion transport [17].

3.3.3 Circuit Fitting

EIS data gathered in this study were fit using a combination of two impedance elements: RQ and a Gerischer element. Both of these elements are commonly used to characterize EIS data obtained from SOC cell tests. The complex non-ohmic response of the cell is primarily attributed to a modified RC circuit where the resistor is in parallel with a capacitance element, characterized by a constant phase element, Q, and is represented by the following equation [2]:

$$(3.5) \qquad Z_{RQ} = \frac{R_{RQ}}{1+(j\omega\tau_{RQ})^n}$$

where

$$(3.6) \qquad \tau_{RQ} = \frac{1}{\omega_{RQ}}$$

and n can have values between 1 (pure capacitor) and 0 (pure resistor). Q elements have no direct physical electrical equivalent, but are characterized by a distribution of relaxation times which result in a depressed semicircular response, as seen in Figure 3.7. This response takes into account the fact that the separation of charge at an interface cannot be modelled as an ideal capacitor, making it commonly in impedance modelling of SOFC components. In the case where n = 1, the resulting impedance simplifies to that of an RC circuit. Gerischer elements are used to model polarization resistance in electrodes where the diffusion losses are significant [38]. Mathematically, this element is described by equation 2:

(3.7)
$$Z_{Ge} = \frac{R_{Ge}}{\sqrt{1+(j\omega\tau_{Ge})^n}}$$

Where

(3.8)
$$\tau_{Ge} = \frac{1}{\omega_{Ge}}$$

Again, n can take values between 0 and 1. This modeling approach is most often attributed to porous materials. An example of the shape of this impedance response can be seen in Figure 3.7. "Best fits" to experimental data were achieved by using a least squares fitting program. The resulting fits and analysis of data is explored further in Chapter 6 of this thesis.
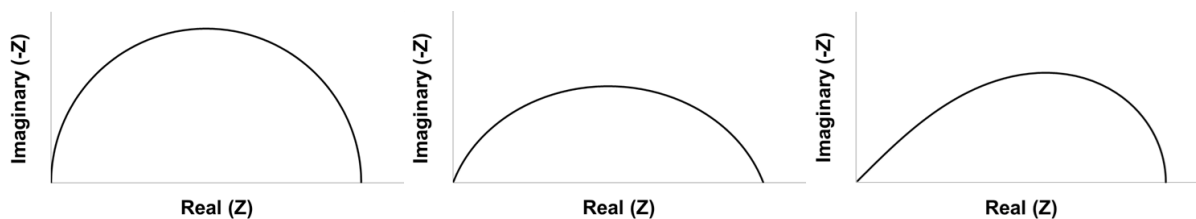
Figure 3.7: Representative shapes for RC (left), RQ (center), and Gerischer (right) circuit elements.

3.3.4   Analysis of Differences in Impedance Spectra

In order to determine definitively if mass transport resistances at high pO_2 were being observed, the subtraction method was utilized to interpret the data. This method is more commonly used to subtract the cathode response from a full cell EIS data set in order to track changes in the anode response or vice versa, as it accentuates small differences between data sets and gives a clearer picture of what sort of changes are occurring. This is particularly noticeable in Bode data (impedance vs. frequency). To obtain subtraction data, the imaginary impedance at any given frequency between two data sets is subtracted from one another. Further information on this analysis method and its use can be found in the literature [41, 42].

3.3.5   Combined Surface Resistance and Coarsening Theory Model

The evolution of R_P over time for SSC-GDC infiltrated symmetric cell cathodes was fit to a combined surface resistance and coarsening kinetics model. Detailed information on the derivation of this model can be found in the literature [34-36], but will be summarized here for completeness.

Assuming that coarsening theory holds, the evolution of a characteristic length scale as a power law in time defined as [35]:

$$(3.9) \qquad l_C^n - l_{C,0}^n = K_D t$$

Where l_C^n grows with time t from an initial size of $l_{C,0}^n$ at a rate defined by the n power [33]. K_D is proportional to a cation diffusion coefficient:

$$(3.10) \qquad K_D = K_{D,0} e^{(-E_D/kT)}$$

Where $K_{D,0}$ is a pre-factor, E_D is an activation energy, k is Boltzmann's constant, and T is the ageing temperature. Size evolution defined by the above equations can then be used to predict the change in infiltrate surface area such that:

$$(3.11) \qquad R_P \propto R_S l$$

At this point, it is necessary to define how the exact relationship between RP and RS is defined. In earlier iterations, the surface resistance model (Equation 3.4) was used as a generalized simplification. This has proven to be much too simplified, as it did not take into account any losses in the system and therefore gave an upper limit to performance which could not be achieved experimentally. The most recent development of the model relates RP to microstructure and materials properties to the transmission-line model [36, 43-47], which has been successfully

applied to infiltrated composite electrodes [36, 46],

$$(3.12) \qquad R_P = \sqrt{\frac{R_S}{\sigma_{ion}a}}\coth\left(L\sqrt{\frac{a}{\sigma_{ion}R_S}}\right)$$

Where σ_{ion} is the effective ionic conductivity of the oxide scaffold (GDC), a is the surface area of the MIEC, and L is the electrode thickness. What is most notable about this equation is that in the limit where the argument is small, when electrodes are exceptionally thin and ionic transport losses are expected to be negligible, coth(x) reduces to 1/x. This results in Equation 3.12 reducing to the form of Equation 3.4.

The value of a, the SSC surface area, is given by the relation $a = fC/l_C$, where C is the surface to volume shape factor ratio that depends on the geometry of the SSC infiltrate particles and f is the SSC volume fraction. For our system, a value of ~6 is used to approximate a hemispherical cap. Combining this expression with Equation 3.9 and Equation 3.12 yields the time dependence of the resistance:

$$(3.13) \qquad R_P = \sqrt{\frac{R_S}{\sigma_{ion}Cf}}(l_{C,0}^n + K_D t)^{1/2n}\coth\left(L(l_{C,0}^n + K_D t)^{-1/2n}\sqrt{\frac{Cf}{\sigma_{ion}R_S}}\right)$$

This equation was used with values measured experimentally in Chapter 6. To determine fit parameters, cells of varying infiltration loading were coarsened at temperatures ranging from 650°C to 800°C. EIS testing for all cells was completed at 600°C and R_P was determined by the

difference between the real intercepts of the Nyquist data, as seen in Figure 3.5. Application of this model to predict long term degradation can be found in Chapter 7.

3.4   SEM Particle Size Analysis

Once infiltration and impedance testing was complete, symmetric cells were fractured, sputtered with 10 nm of Au and the cross-section was imaged using either a Hitachi S-4800-II or Hitachi SU8030 microscope. Size measurements of infiltrate material could not be determined within the cathode structure due to both the comparable size of infiltrate particles to the scaffold and the lack of phase contrast between the scaffold and infiltrate material. To circumvent this issue, infiltrate particle sizes were taken from SEM images taken at the electrolyte-cathode interface, where SSC nanoparticles could be best differentiated from the scaffold and accurately measured. Particle diameters were averaged over a minimum of 50 infiltrated particles from at least 3 different regions along the interface. A sampling of these images is shown in Figure 3.8.

3.4.1   Simple Infiltrated Microstructure Polarization Loss Estimation (SIMPLE)

As detailed further in Chapter 7, small changes in infiltrate particle size greatly affect the resulting polarization resistance of these infiltrated cathodes. For this reason, it is important to determine the reproducibility of particle size, as well as whether the size of the infiltrated particles could be tuned and optimized experimentally.

For much of the analysis completed over the course of this thesis, a reliable estimate of the initial average particle size, $l_{C,0}^n$, is necessary. To determine this value, the concentration of SSC

material was varied by both infiltration cycle (μL of solution infiltrated as well as varied cathode thickness) plus varying the number of infiltration cycles. For the purposes of this study, one infiltration cycle was taken to consist of deposition of nitrate solution onto the ionic scaffold (GDC), gelation of solution at 60°C, and synthesis at 800°C for 1 h. Table A1 lists the experimental design and results.
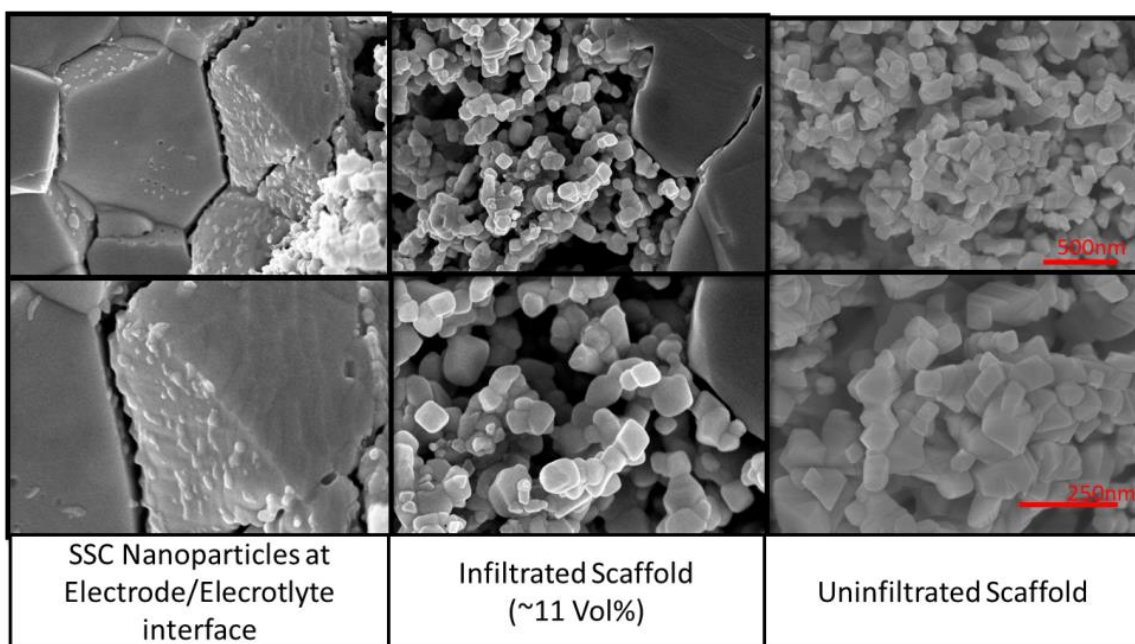
Figure 3.8: Representative SEM images of infiltrated cathodes. Top and Bottom images are of the same area of the cell, but taken at different magnifications. Left images show the electrode/electrolyte interface with isolated nanoparticles of SSC on the GDC electrolyte. Center images shows a GDC scaffold infiltrated with ~11 vol% SSC. There is no phase contrast between the scaffold and infiltrate material. Right images show an example of an uninfiltrated GDC scaffold for comparison.

Initial results based on the mean and mode of particle sizes measured made it appear that varying concentration of infiltrate solution allowed for systematic changes in particle size.

Evidence of this can also be seen in Figure 3.10. Further investigation showed that while average particle sizes decreased with increasing infiltration solution concentration, most samples were within standard deviation of one another, as noted in Table A1, with the exception of cells with very high infiltration solution concentrations per infiltration cycle, where there was a marked decrease in particle size.

Subsequent cells produced over the course of this thesis utilized a "max infiltration" methodology where 2 M nitrate solution was infiltrated into the scaffold structure until the pore structure was completely filled. Excess nitrate solution was blotted off prior to gelation and high temperature decomposition. Vol% infiltration loadings were calculated based on the weight uptake of SSC on the cells and the known density of SSC. This method was used to ensure that the concentration of solution infiltrated per unit volume was similar for all other cell produced, regardless of variation in scaffold thickness.
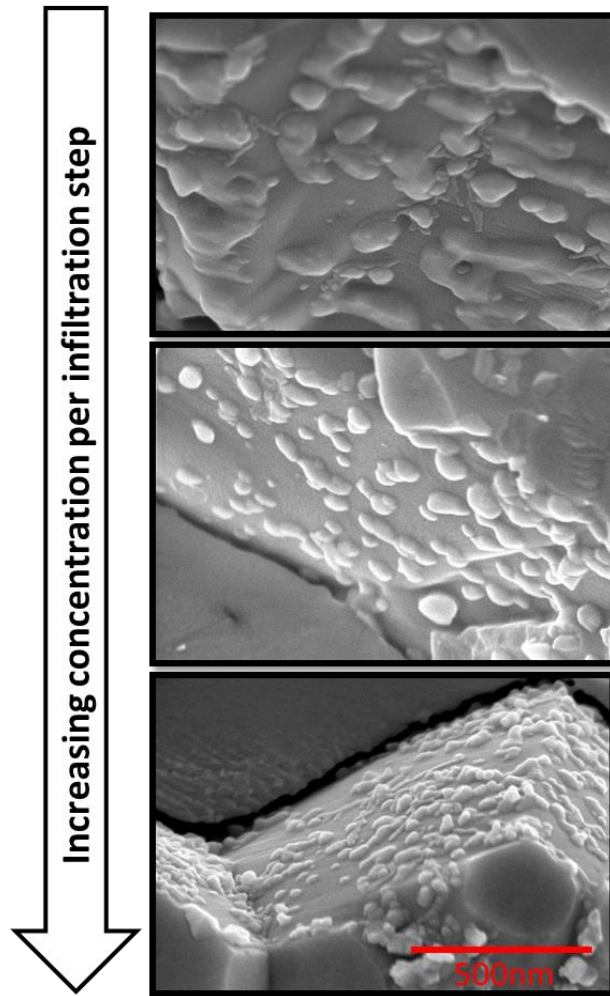
Figure 3.9: SEM micrographs of infiltrate particles produced with increasing concentration per infiltration step

Chapter 4

Polarization Resistance Prediction Using the Simple Infiltrated Microstructure Polarization Loss Estimation Method

A study using symmetric cells consisting of $La_{0.6}Sr_{0.4}Co_{0.2}Fe_{0.8}O_{3-\delta}$ (LSCF) nanoparticles infiltrated into $Ce_{0.9}Gd_{0.1}O_{1.95}$ (GDC) scaffolds was completed in order to verify the validity of a modified Tanner-Fung-Virkar (TFV) model, the Simple Infiltrated Microstructure Polarization Loss Estimation (SIMPLE) Model [17, 40], for use in predicting initial performance of infiltrated nano-structured cathodes. This model accounts for both surface effects and bulk ionic transport through the cathode layer, and gives a more accurate prediction of polarization losses than surface resistance models which do not take into account losses associated with ionic transport.

A series of symmetric cell cathodes were systematically infiltrated with 1 μl of 0.5 M LSCF citric acid nitrate solution with increasing numbers of infiltration cycles to produce samples with variable mixed ionic and electronic conducting (MIEC) particle infiltrate loadings. By determining the average infiltrate particle size, known MIEC loading, and known cathode volume, the volume percent of LSCF was determined and samples were compared using this metric to their measured polarization resistance (R_P) values. Measured microstructural parameters and materials properties gathered from literature sources [10, 11, 17] were employed as inputs for the SIMPLE model to obtain predictions on polarization losses to compare with experimentally gathered data.

A large portion of the contents of this chapter have been co-authored and published with Dr. Jason Nicholas as first author of this work. Additional work published alongside this study was done on GDC-SSC infiltrated cathodes, which is not reported in this thesis, was conducted by

Ms. Lin Wang [17].

4.1 Experimental Methods

GDC-LSCF symmetric cell cathodes were prepared via sol-gel infiltration and tested using electrochemical impedance spectroscopy (EIS) as outlined in Chapter 3 of this dissertation. Briefly, cells were produced by screen printing a porous GDC layer with a footprint size of 0.5 cm^2 on both sides of a dense GDC electrolyte support, and firing at 1100ºC for 4 h. The resulting porous scaffold layers, were then infiltrated with a sol-gel solution consisting of Millipore water solvent containing metal nitrates with concentrations designed to produce LSCF. Citric acid was added to the solution in a 1:1 molar ratio of (metals : citric acid) to act as a chelating agent to ensure the production of single phase SSC upon decomposition of the nitrate solution at 800°C in air for 1 hour. The wet infiltration and decomposition step was repeated as many times as necessary in order to obtain the desired loading of LSCF. Post-test analysis of the cross-section via scanning electron microscopy revealed the particle size to be ~50 nm, as seen in Figure 4.1. Time at operating temperature was considered sufficiently low (> 24 h) so as to not induce considerable increases in particle size over the course of EIS testing, allowing the measured particle size to be used in subsequent calculations.

Details on additional microstructural properties (cathode thickness, scaffold surface area, SSC surface area) were calculated using data obtained through profilometry measurements and microstructure estimates pulled from SEM image analysis. Expected values of R_P were obtained through calculations based on the SIMPLE model. More information on this model can be found

in Chapter 3 of this dissertation.
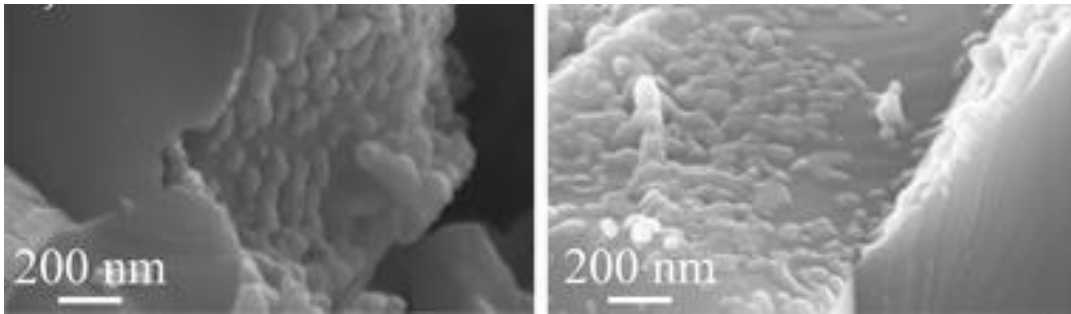
Figure 4.1: Representative images of LSCF particles that were measured to predict polarization resistance. Particle sizes are ~ 50 nm in diameter. Figure adapted from [17] with permission.

4.2   Results and Discussion

SEM images of these cathodes revealed networks of LSCF particles with ~50 nm size coating the porous GDC structure. EIS measurements of samples with symmetrical LSCF-GDC cathodes on GDC electrolytes showed that increasing the LSCF volume infiltrated decreased cathode R_P, to as low as 0.23 Ω cm^2 at 600°C for 12 vol% infiltrated LSCF. R_P predictions were made assuming that the mixed-conducting LSCF surface effect and bulk ionic transport through the cathode layer were the major factors limiting polarization, using literature values from Baumann of LSCF surface resistance [11] and LSCF surface areas estimated from SEM images. The two methods used are the Surface Resistance Model (Equation 4.1) and the SIMPLE Model (Equation 4.2) more thoroughly explained in Chapter 3.

(4.1)
$$Rp = \frac{Rs_{Inf}}{A_{Inf}/A_{FP}}$$

$$(4.2) \qquad R_P = \frac{r\left(\frac{R_S A_{Sc}}{A_{Inf}}\right)}{\left(\frac{1+\beta}{1+\beta\,\exp\left(\frac{-2h}{\alpha}\right)}\right)r(1-p)\exp\left(\frac{-h}{\alpha}\right)+\frac{\left(1+\beta\left(\frac{-h}{\alpha}\right)\right)}{\left(1+\beta\left(\frac{-2h}{\alpha}\right)\right)}\alpha\left(1-\exp\left(\frac{-h}{\alpha}\right)\right)+pr}$$

It should be noted that there were not significant differences between the calculated values of R$_P$ for either model, as shown in Figure 4.2, and the predicted and measured values using both the Surface Resistance (dashed lines) and SIMPLE (solid lines) models appear to agree over a wide range of LSCF volume fractions tested. Experimental values for polarization resistance deviate widely from SIMPLE model predictions at low infiltration loadings. While not ideal, this is to be expected since the model assumes complete electrical connectivity throughout the electrode. At low infiltration loadings, a large fraction of infiltrated MIEC are comprised of isolated particles which are not electrically connected and are therefore not electrochemically active in the fuel cell. Any material which is not electrically connected in the cell will not positively contribute to the polarization resistance of the electrode, leading to inaccurate estimations of R$_P$. To avoid this effect, it is important to use an infiltration loading that is high enough to allow percolation of electrons through the length of the microstructure, in this case > 5 vol% infiltrate loading.

At high infiltration loadings, the data appear to "beat" the estimation for polarization resistance given by the SIMPLE model using Baumann values. This result is unexpected as the model only takes into account losses associated with surface effect and bulk ionic transport through the cathode layer, and therefore should give a "best performance" estimate for the microstructure

defined. Model predictions were made using the extrapolated 600-750°C LSCF R_S values from Baumann *et al.* [11] and extrapolated 425-550°C LSCF Rs values from Xiong *et al* [10]. There is roughly an order of magnitude difference in R_S values depending on which source is used, so it should come as no surprise that the experimental data lies approximately between model predictions using either source material. Both models are sensitive to changes in R_S and this result confirms the need for accurate materials property data for polarization loss estimation to be a useful tool in predicting the performance of novel nano-scaled microstructure and materials systems.
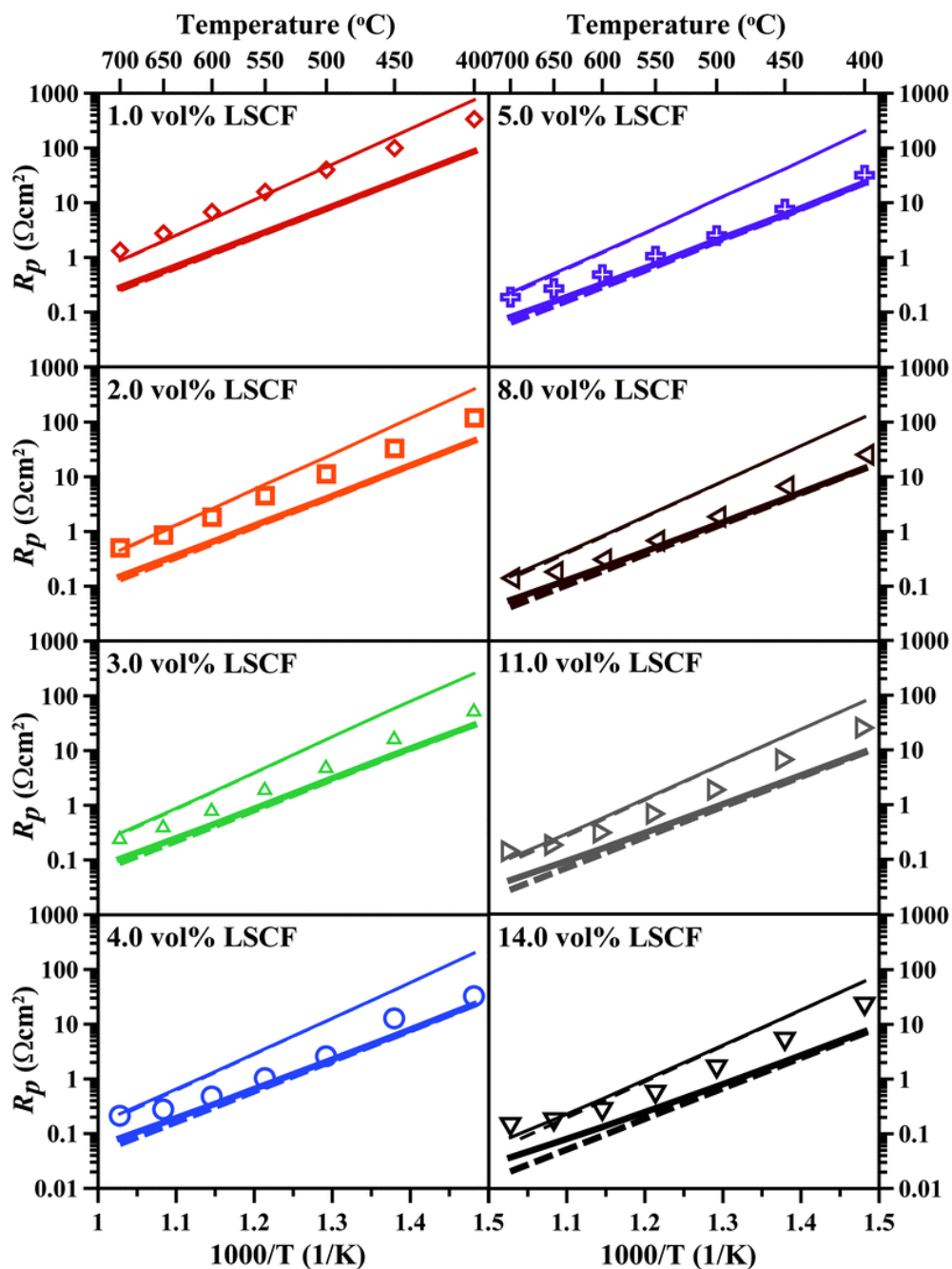
Figure 3.2: Comparisons of measured LSCF–GDC polarization resistances (symbols) to surface resistance (dashed line) and SIMPLE model predictions (solid lines) obtained using intrinsic LSCF surface resistance values from [11] (thin lines) and [10] (thick lines). Measured resistance errors are less than the size of the symbols. Image taken [17] from with permission.

4.3 Conclusions

In summary, the SIMPLE model was used to predict R_P values for LSCF-GDC infiltrated nano-composite symmetric cell cathodes and was found to fit experimental data to within an order of magnitude for samples infiltrated at ~5-15 vol% LSCF. For heavily infiltrated samples, use of the SIMPLE model can be used to determine a "best performance" estimate for a nano-infiltrated composite cathode. Data obtained at low infiltration loading (< 5 vol%) deviated from the model due to the prevalence of isolated and inactive regions. Furthermore, the accuracy of SIMPLE model estimations is dependent on the use of accurate materials property data on the constituent materials used in the cathode system. For polarization loss estimation to be a viable method of identifying high performance material systems and parameters, accurate values for surface and bulk materials properties must be obtained.

Acknowledgements

Chapter 5

Electrochemical Impedance Spectroscopy Analysis of Infiltrated $Sm_{0.5}Sr_{0.5}CoO_{3-\delta}$ Solid Oxide Fuel Cell Cathodes

Most studies on infiltrated cathodes are focused on improvement of polarization resistance (R_P) values as this is often considered the best measure for comparing cathode performance between systems. This has led to large number of publications with varying performance reported for what appear to be the same cathode systems [7, 12]. Due to the novel microstructure inherent in infiltrated cathodes, performance variation can be caused by changing the material systems being studied [7, 12], varying infiltration loading (vol% scaffold : vol% infiltrated nanoparticles) [17, 36, 39], as well as scaffold and infiltrate microstructures [18, 30]. The general trend in the literature is to strive for very fine scaffold microstructures to increase available surface area available for nano-particle deposition. Infiltration loadings are then done to provide full surface area coverage to maximize the available active area for the oxygen reduction reaction.

Basic calculations to determine the performance associated with infiltrated microstructures typically assume that most, if not all, of the resultant R_P value from an infiltrated cathode is due to the properties of the infiltrated material and the available surface area of the cathode microstructure. Work has been completed to model the polarization loss behavior more accurately [17, 19, 20, 37, 39, 48], with limitations being on the availability of accurate materials parameters available for such calculations. Additionally, with decreasing characteristic sizes of both infiltrate materials and their corresponding scaffold, additional loss mechanisms from mass transport and grain boundaries may have an important role in electrode design. An in-depth experimental analysis of

data with changing infiltration loading, microstructure, temperature, and pO_2 has not been completed for infiltrated cathodes, though there is literature is available on single-phase porous MIEC cathodes [40, 49-54].

In this study, symmetric-cathode cells with GDC electrolytes were prepared via infiltration of aqueous nitrate solutions to form SSC nano-particle coatings in porous GDC scaffolds with varying SSC infiltrate loading. Electrochemical impedance spectroscopy (EIS) measurements were completed for cells with different SSC loadings, at temperatures ranging from 400°C - 750°C and oxygen partial pressures from 100-1% O_2. The data were fit using two different equivalent circuit models, featuring either an RQ element or a Gerischer impedance element to characterize mid-frequency responses. Equivalent circuit fitting allows for the isolation of different cathode responses. The results indicate that the primary source of cathode resistance is associated with oxygen surface exchange and bulk diffusion, while gas diffusion and grain boundary resistances, either within the cathode GDC phase or the GDC electrolyte, were also observed to have measurable influence on R_P.

5.1   Experimental Methods

The symmetric cathode cells tested in this study were prepared using the procedure described in Chapter 3. Briefly, cells were produced by screen printing a porous GDC layer with a footprint size of 0.5 cm^2 on both sides of a dense GDC electrolyte support, and firing at 1100°C for 4 h. The resulting porous scaffold layers were then infiltrated with a sol-gel solution consisting of Millipore water solvent containing metal nitrates with concentrations designed to produce

$Sr_{0.5}Sm_{0.5}CoO_{3-\delta}$ (SSC). Citric acid was added to the solution in a 1:1 molar ratio of (metals : citric acid) to act as a chelating agent to ensure the production of single-phase SSC upon decomposition of the nitrate solution at 800°C in air for 1 hour. The wet infiltration and decomposition step was repeated as many times as necessary in order to obtain the desired loading of SSC, as measured by weighing the cells before and after infiltration. The present cathodes had 6, 15, or 20 vol% SSC; these amounts were selected based on prior work [17] as being representative of low, medium, and high loading levels. As described in Chapter 3, this procedure results in SSC particles of ~50 nm diameter decorating GDC scaffold surfaces. Prior to electrochemical testing, $La_{0.85}Sr_{0.15}MnO_{3-\delta}$ LSM current collectors were screen printed on top of the infiltrated cathode layer and fired in air at 800°C for 2 hours.

Cells were mounted in a pressure Au contact rig [40] and were tested under flowing O_2 gas balanced with Ar gas, at O_2 fractions from 1-100% at 1 atm. EIS measurements were carried out using a Solartron 1260 frequency response analyzer at frequencies between 10-1 and 106 Hz. Note that complete sets of pO_2 and temperature variation tests were done on each of the cells, so internally consistent data sets were obtained avoiding any issues with sample-to-sample variations. Temperature was varied from 750°C to 400°C in 50°C increments, and was completed in order of highest to lowest temperature, with the complete set of pO_2 variation tested before decreasing in temperature. This was done so that any particle coarsening was completed at the beginning of the tests, minimizing cathode variations within a given data set. Some test conditions were repeated at intervals during the testing process, and it was found that cell performance was stable throughout at any given temperature setting.

5.2   Analysis of Differences in Impedance Spectra

As a first step taken to determine the number of loss mechanisms which are evolving in our system, an analysis of differences in impedance spectra (ADIS) was completed on pO_2 and temperature data. Another name for this technique is the subtraction method. This method is more commonly used to subtract the cathode response from full cell EIS data sets in order to track changes in the anode response or vice versa [41, 42]. Small differences between data sets are accentuated and it gives a clearer picture of what sort of changes are occurring and at what frequencies they are evolving. Further information on how this technique is implemented can be found in Chapter 3 of this dissertation and in the literature [41, 42]. Figure 5.1 shows a bode plot of the subtraction data for a high-loading sample (20 vol% SSC) at 600°C with varying pO_2. Data obtained from flowing 100% O_2 is used as the baseline, which is subtracted from all other EIS spectra. Two distinct peaks as shown are visible in the subtracted data. This shows that there are two different mechanisms that are likely evolving with pO_2: mass transport and surface exchange reaction.
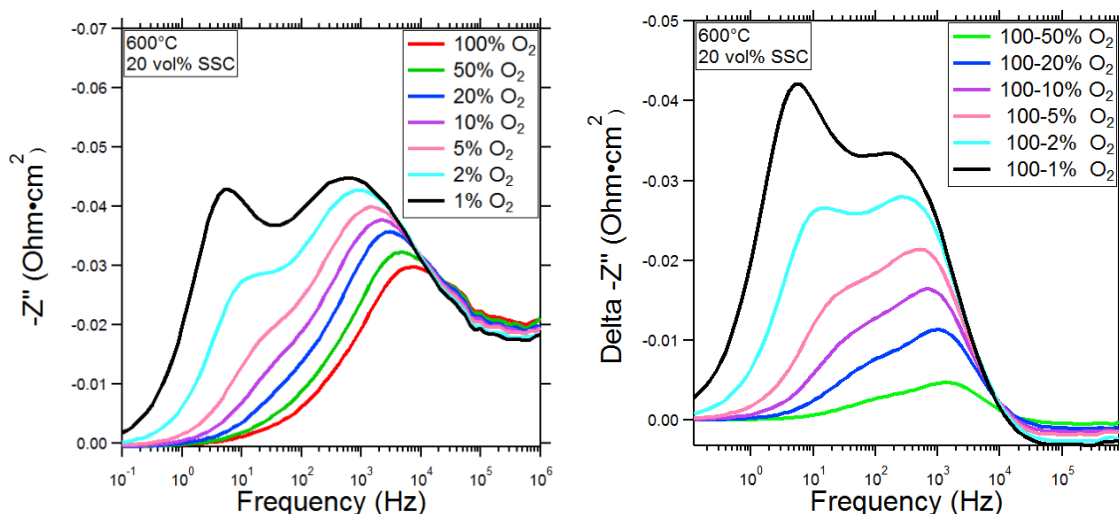
Figure 5.1: a) Bode plot showing for a high loading sample (20 vol% SSC) at 600°C with varying pO_2 balanced with Argon and b) subtraction of the same data set. Data obtained from flowing 100% O_2 is used as the baseline which is subtracted from all other EIS spectra. Two peaks are clearly seen evolving with changing pO_2 at all O_2%.

It is important to note that we only see two processes changing and that any other processes occurring in the cell do not appear to have a pO_2 dependence. In order to confirm the responses observed, impedance fitting is necessary. Additionally, while this is a powerful method in determining the presence of loss mechanisms in EIS data, it is not possible to fit these losses directly from subtraction data. This is because any shift in the characteristic frequency of these loss mechanisms will lead to abnormally wide peaks which cannot be accurately fitted by circuit analysis in a meaningful way.

5.3 Impedance Model Fitting

EIS data gathered in this study were found to fit acceptably using two different equivalent

circuit models: one containing an RQ element and the other a "Gerischer" element to represent the primary impedance response. Circuit diagrams for both models are provided in Figure 5.2.

Definitions of RQ and Gerischer circuit elements can be found in Chapter 3 of this dissertation. To summarize briefly, RQ fits take into account minor variations within a cell, unlike RC circuit elements, and is common in impedance modeling of SOFC components. The impedance response is characterized by a depressed semi-circle in a Nyquist plot (Figure 5.3). Gerischer elements are used to model polarization resistance in electrodes where diffusion losses are significant and are frequently attributed to the response expected from porous materials. An example of the shape of this impedance response can be seen in Figure 5.3.
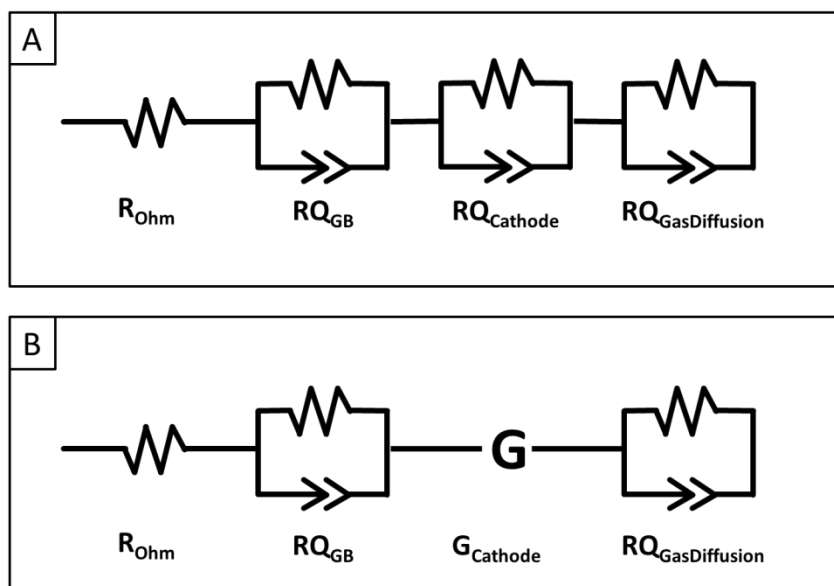
Figure 5.2: Circuit diagrams for the two fitting models used in this study. A) Cathode characterized by an RQ impedance response to electrochemical losses. B) Cathode characterized by a Gerischer impedance response to electrochemical losses. Both models include considerations for ohmic, grain boundary, and gas diffusion losses.
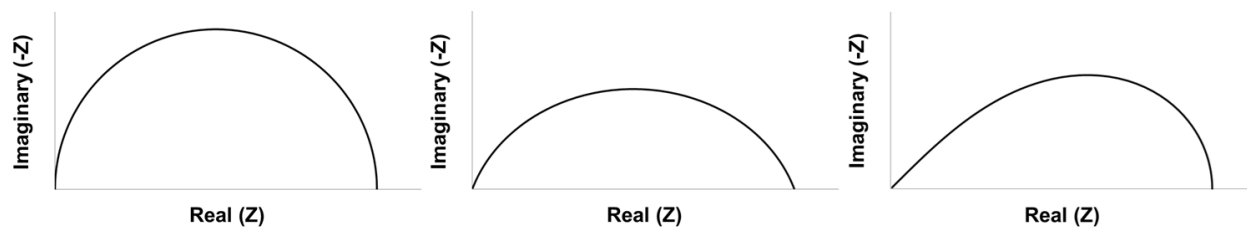
Figure 4.3: Representative shapes for RC (left), RQ (center), and Gerischer (right) circuit elements.

Both models utilize a resistor to model the ohmic resistance of the electrolyte and RQ elements to describe both grain boundary resistance and gas diffusion losses. In the case of RQ$_{GasDiffusion}$, the value of $\alpha \approx 1$, which is equivalent to an RC circuit and is expected for this impedance response [55].

"Best fits" were achieved by using a least squares fitting program and confirming that the fits evolved within each changing variable for the data set being fit, as well as logically between an entire set of data comparing pO$_2$ variation and temperature variation. As can be seen in Figure 5.4, both models give reasonable fits.
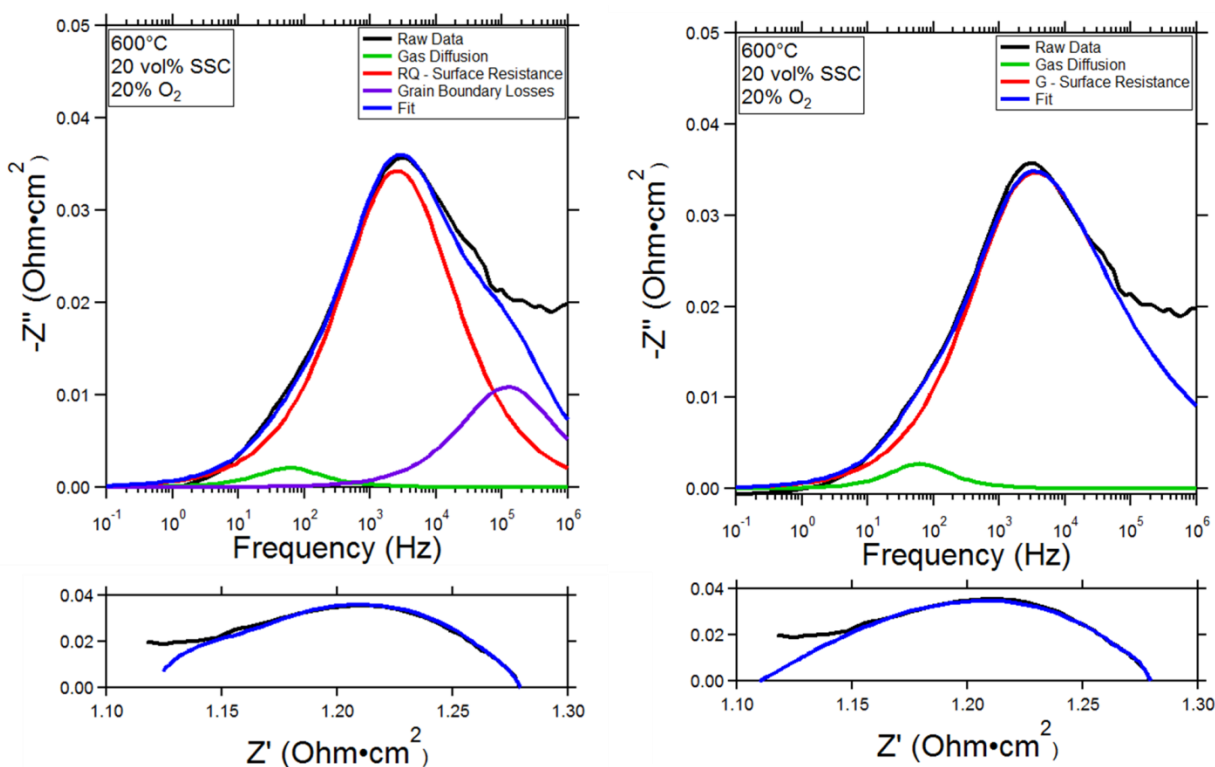
Figure 5.4: Representative fits for RQ and Gerischer fits. Both models give reasonable fits for the data presented.

5.4   EIS Data and Impedance Fitting Results

5.4.1   Effect of SSC Loading

Three infiltration loadings were used in this study: 6 vol%, 15 vol%, and 20 vol%, where vol% loading is defined by the infiltrate material volume (SSC) with respect to the total volume of the cathode. These loadings were chosen as representative cases of very low, average, and high infiltration volumes, in order to characterize the effect of loading on the resulting EIS spectra. Infiltration loading changes not only the SSC surface area, particle connectivity, etc., but also impacts the pore volume, which is displaced by the SSC.

Figure 5.5 shows Bode and Nyquist plots of the low, average, and high infiltration EIS spectra tested at 600ºC and 20% O_2. The average and high loading samples show what appear to be a single peak at a frequency that decreases from ~ 10^4 to ~ 10^3 Hz with increasing loading. The 20 vol% loading sample showing a lower R_P value than the 15 vol% sample, as expected if increasing the SSC loading results in increased SSC surface area [17-19, 29, 37, 39, 48].

In contrast, the 6 vol% sample is very different, exhibiting two responses, one at ~ 10^2 Hz and the other at 10^5 Hz, both of which are much different than the single response seen at higher loadings. Based on prior SSC infiltration results, [17, 48] the relatively high R_P is expected, given the lower SSC surface area combined with the likelihood that a significant fraction of SSC particles are electrically isolated from the current collector, and hence electrochemically inactive. In this case, the cathode layer could be acting more like an extension of the electrolyte layer. Although one might suggest that the lower frequency peak corresponds to a contribution from the electrochemical activity of the LSM current collector, this is unlikely because the polarization resistance is much lower than that expected from an LSM cathode. Considering the high resistance and atypical results from the 6 vol% sample, this case is not considered further in this study.
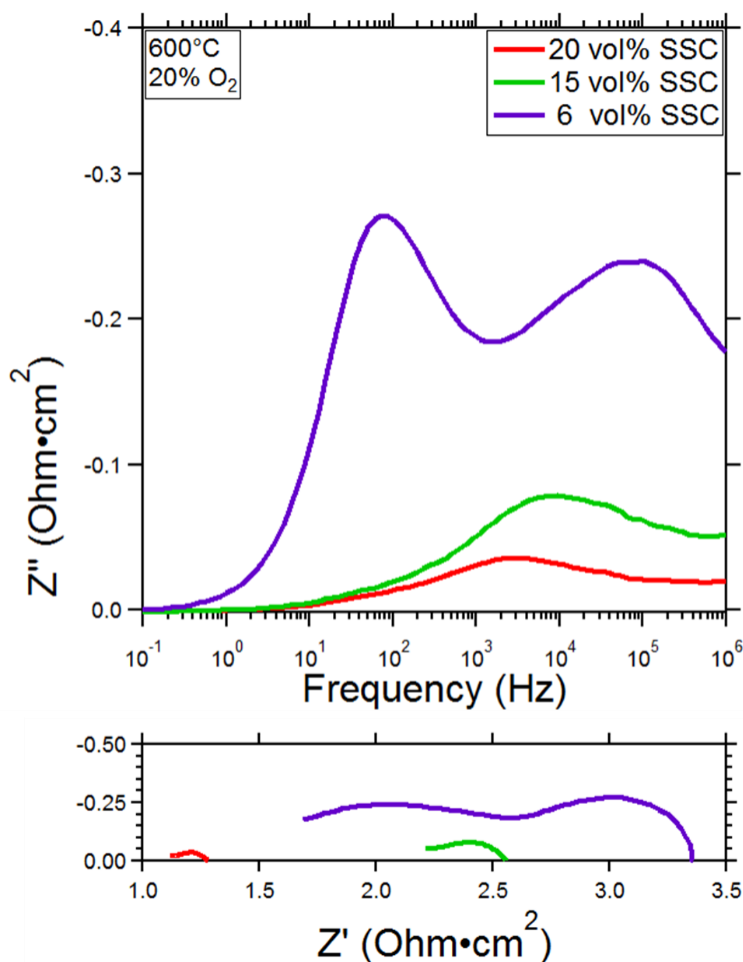
Figure 5.5: Bode (top) and nyquist plots (bottom) from high (20%) mid (15%) and low (6%) loading SSC infiltrated samples tested at 600C in 20% O_2. Variations in $R\Omega$, seen in the nyquist plot, is due to electrolyte thickness, which was not held constant in this study. Low loading samples showed atypical behavior, particularly at low frequencies.

As mentioned earlier, infiltration loading also effectively changes the microstructure of these cathodes due to pore volume being displaced by MIEC nanoparticles. As pore volume decreases, mass transport losses can have a larger effect on polarization resistances and significantly contribute to R_P. Additionally, it is possible for some infiltrated areas to become

isolated and inactive, further decreasing performance. Highly infiltrated samples showed decreased surface exchange/diffusion losses, but also showed a small increase in mass transport losses, which became visible in samples tested at high temperatures and intermediate/low pO_2 concentrations (< 20%). In order to combat this effect, it will be necessary to vary the microstructure so that there is a larger pore volume in the initial scaffold. This may decrease performance slightly, as scaffold surface area will likely be sacrificed. Further observations on the subject of scaffold microstructure with infiltration loading held constant can be found in the literature [18, 30].

5.4.2   Temperature Dependence

Figure 5.6 shows representative impedance data and their corresponding Gerischer fits for the 20 vol% loading sample and 20% O_2 atmospheric condition between 550ºC and 700ºC. Trends to note are the strong temperature dependence that R_Ω and R_G exhibit. The response at > 105 Hz, discussed further below, also decreased in magnitude with increasing temperature, but more slowly than R_G, such that it became a larger portion of the total resistance at higher temperature. The upturn in the data at high frequencies, particularly noticeable at low temperatures, confirm that at least part of the resistance measured in these cells is due to this high frequency response and not entirely from the oxygen surface exchange reaction. Finally, a low frequency response is noted in tests at high temperatures (600-700ºC). This contribution, which does not appear to vary with temperature, is only measurable at the highest temperature where the Gerischer response is sufficiently small. It does not appear to vary with temperature, and so it is likely associated with

gas diffusion concentration polarization.
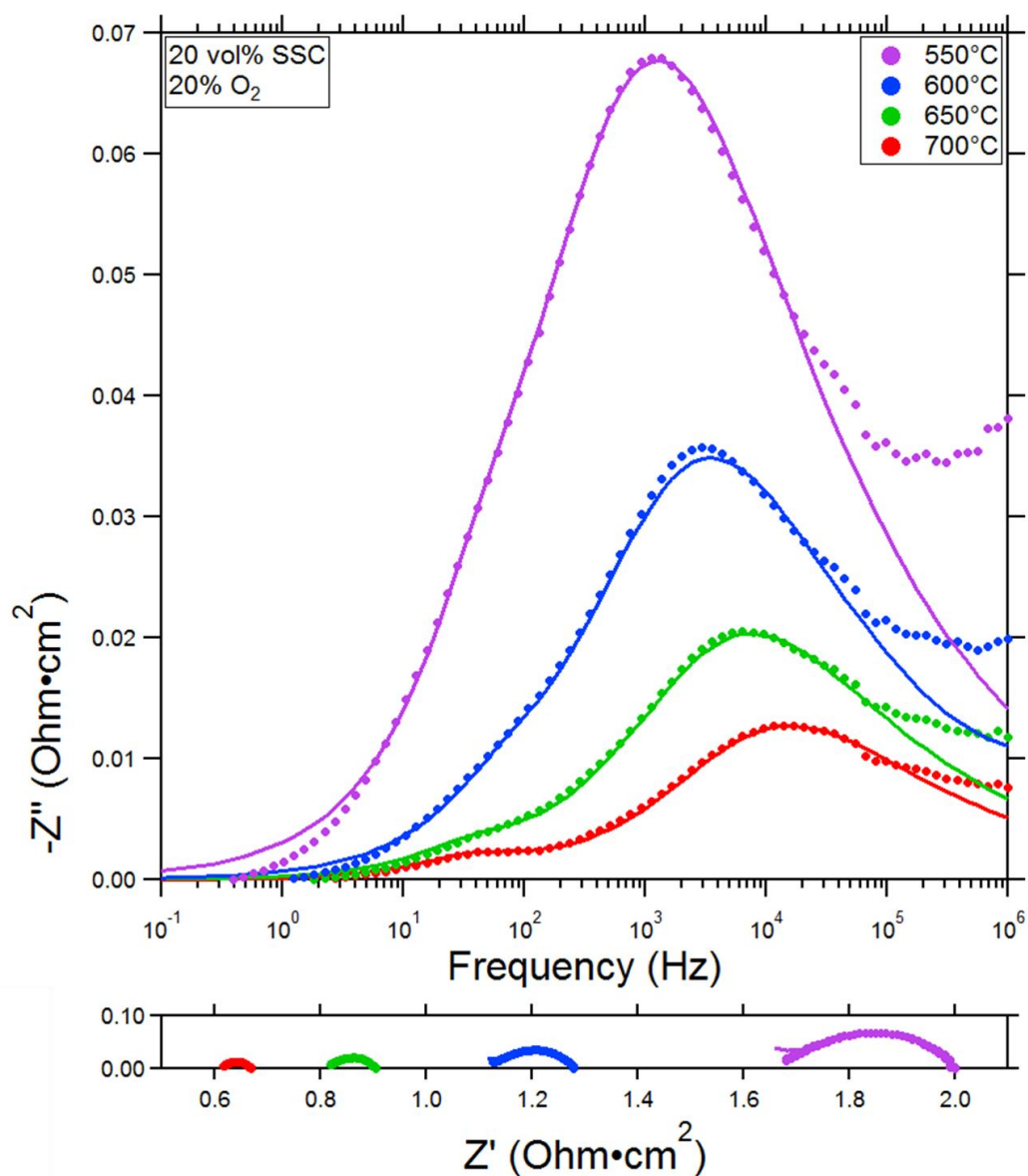
Figure 5.6: Bode (top) and nyquist (bottom) of a 20 vol% infiltrated cathode tested at 550-700ºC and 20% O₂ content. Data from temperatures below 550ºC is not shown at the impedance response was so large as to dwarf high temperature data.

Figure 5.7 is a plot showing the temperature dependence of R_G with respect to temperature for both the high and mid loading samples, based on fits using a Gerischer element. R_G increases with decreasing temperature following an Arrhenius behavior with activation energies of ~0.64 eV for 15 vol % SSC and 0.84 eV for 20 vol % SSC. Figure 5.7 also shows the values obtained assuming an RQ element in the equivalent circuit instead of a Gerischer element. Other than a minor offset in the resistance value reported, both circuit models fit the data equally well and yield the same activation energies as the Gerischer model. While it might normally be possible to distinguish between Gerischer and RQ responses based on shape, in the present data there is significant overlap with the higher-frequency response, making deconvolution difficult. Regardless of the equivalent circuits used, however, Figure 5.7 shows that the model used has little impact on extracting the resulting temperature dependence. This is also the case for other variables, including the SSC loading and pO_2.

Although the cathode polarization is shown to be dominated by oxygen surface exchange and oxygen ion diffusion in the cathode at mid-frequencies, there is also a non-negligible contribution observed at high frequencies. Additionally, the magnitude of this response appears to be independent of infiltrate loading, though it is difficult to track due to its overlap with the lower frequency response. Since only a small portion of this high frequency response is seen in the data, it is not possible to achieve an accurate fit.

It is possible that this response is associated with grain boundary resistances in the electrolyte material. Another possibility is that this grain boundary resistance is associated not with the electrolyte layer, but the cathode itself. This could either be associated with the grain

boundary resistance of the GDC scaffold layer, or from charge transfer between the SSC infiltrate particles and the GDC scaffold layer. Further tests with modified microstructures, as well as EIS tests at much higher frequencies will be necessary to confirm the source of this resistance.
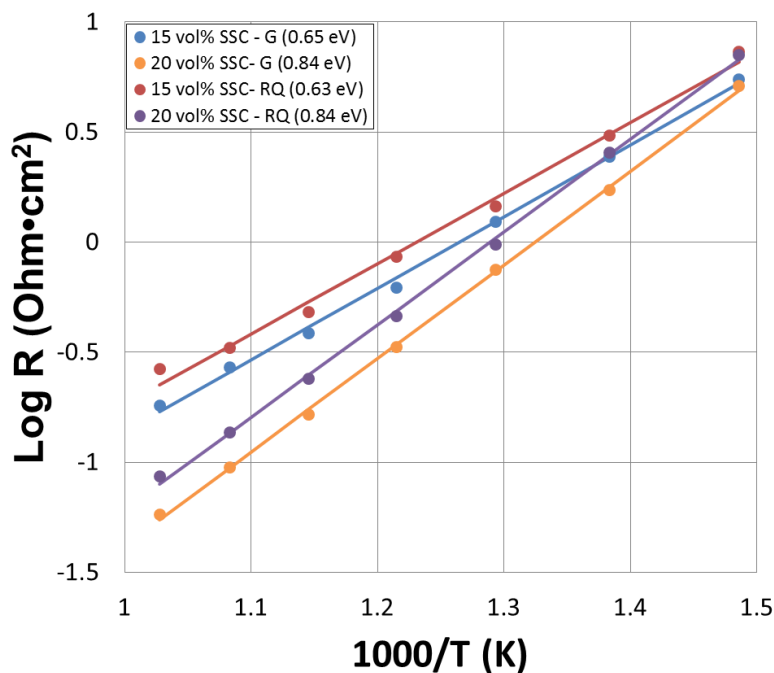
Figure 5.7: Arrhenius plot of R_P vs. 1000/T modelled with both G and RQ elements at 20% O_2. Other than a minor offset in the resistance value reported, both circuit models fit the data with very similar results and gave activation energies of ~0.64 eV and 0.84 eV for 15 and 20 vol % SSC loadings respectively.

5.4.3   Digital Image Correlation

Figure 5.8 shows an example of EIS data from the 20 vol % SSC infiltrate loading cell tested at 600°C at varying levels of pO$_2$. The main oxygen exchange/diffusion response grows in magnitude and shifts to lower frequency with decreasing pO$_2$. A lower-frequency response

becomes visible at pO_2 below ~ 0.1 atm, growing rapidly and shifting to lower frequency with decreasing pO_2. This response could not be reliably fit above 20% O_2 and below 500°C where it was overwhelmed by the oxygen exchange/diffusion response. Figure 5.9 shows a plot of the resistances used in the Gerischer and RQ elements to fit these data. Both were fit well with simple power law dependences $(pO_2)^n$, where n = -0.12 for the oxygen exchange/diffusion response and n = -1.0 for the lower-frequency response. The low n value for the oxygen exchange/diffusion response is consistent with prior reports for many MIEC cathode materials [41, 56]. The lower-frequency response was identified as gas diffusion concentration polarization, based on the power law dependence of -1 and its lack of any variation with temperature [41].
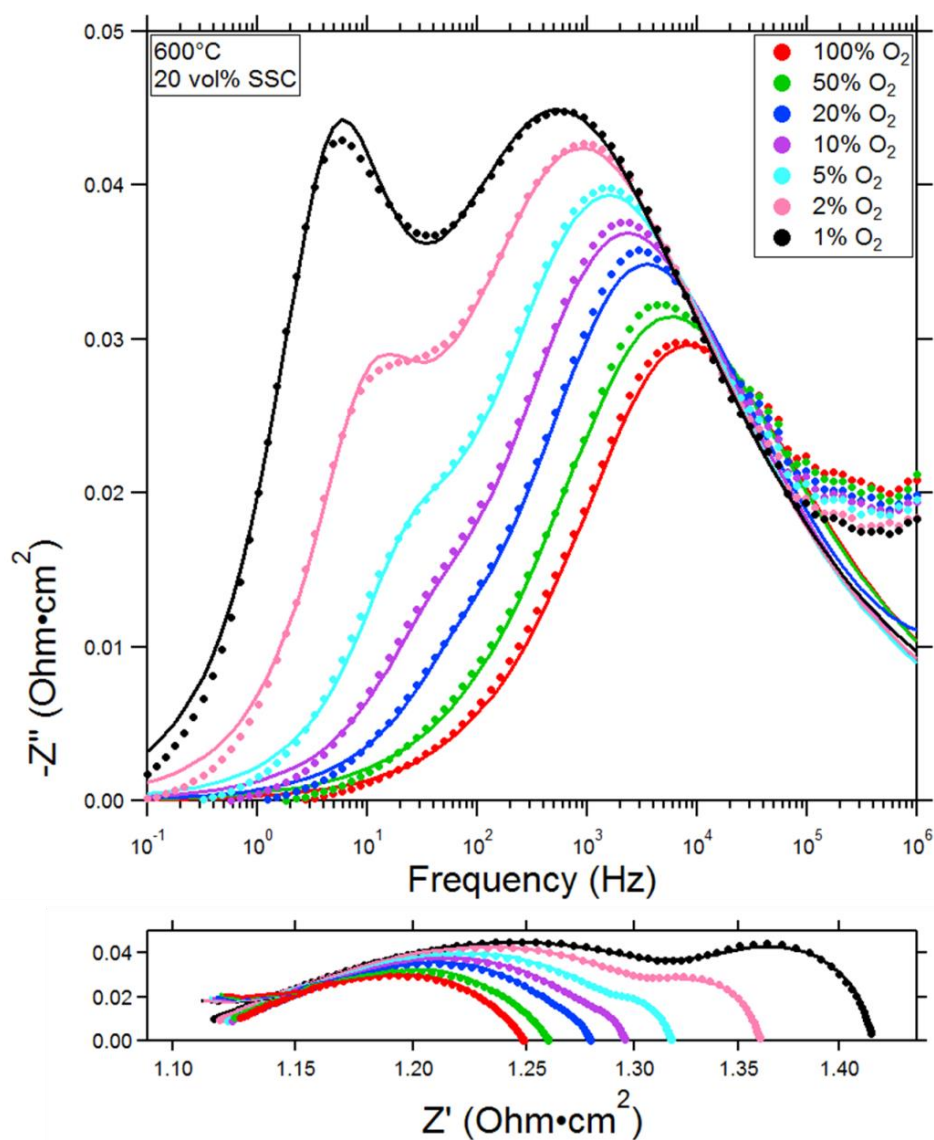
Figure 5.8: Bode (top) and Nyquist (bottom) of a 20 vol% infiltrated cathode tested at 600°C with varying O_2 partial pressure. Low frequency contributions due to oxygen diffusion losses are apparent in the low frequency regime.
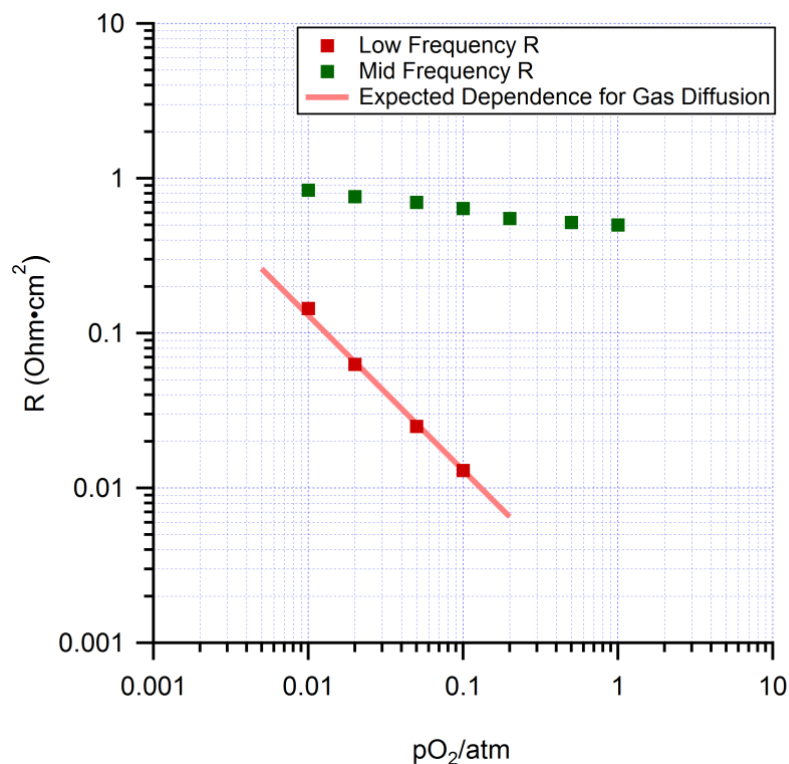
Figure 5.9: Plot of RQ resistances measured against varying pO_2 for the 20 vol% SSC-GDC infiltrated sample. Low frequency contributions were only measurable between 1 and 10% O_2 conditions, and fit a power law dependence of -1 which is expected for gas diffusion losses.

5.5   Conclusions

Electrochemical impedance spectroscopy measurements were completed between 750°C and 400°C to simulate intermediate and low temperature operation on samples of varying infiltration loading. Electrical impedance spectroscopy with pO_2 variation was used to gain insights into electrochemical processes. EIS data were fit using both RQ elements and Gerischer elements. Both equivalent circuits gave reasonable fits within standard operating conditions.

Regardless of the fitting model used, all samples exhibited a high, mid, and low frequency response, which corresponded to mass transport, oxygen surface exchange reaction, and a

microstructure based contribution. The microstructural response can be attributed to grain boundary resistances in the electrolyte material, grain boundary resistance of the GDC scaffold layer, from charge transfer between the SSC infiltrate particles and the GDC scaffold layer, or a combination of these. Further tests with modified microstructures, as well as EIS tests which extend to higher frequencies if such equipment is becomes available will be necessary to confirm the source of this resistance.

Infiltration loading effectively changes the microstructure of these cathodes because pore volume is being displaced by MIEC nanoparticles. While high infiltration volumes will yield lower polarization resistances due to a higher active surface area/volume, mass transport resistances increase due to a reducing pore volume. Mass transport effects were verified in our data even for samples tested at pO_2 greater than 10% O_2. In order to combat this effect, it will be necessary to vary the microstructure so that there is a larger pore volume in the initial scaffold. This may decrease performance slightly, as scaffold surface area will likely be sacrificed.

5.6   Acknowledgements

Chapter 6

Accelerated Testing of $Sm_{0.5}Sr_{0.5}CoO_{3-\delta}$ Infiltrated Scaffolds

Long-term stability is a concern for all SOFC materials systems. Between the harsh testing environment which includes and both highly oxidizing and highly reducing conditions, high temperature operation, 750–850 °C for current state of the art SOCs, and long expected lifetimes, >40,000 hours, there are a number of degradation pathways that need to be explored to determine the viability of both the SOFC system generally and the specific material components utilized in the SOFC itself. To mitigate many of these issues, reduction of the operating temperature to a range of 400°C-600°C is being explored [57]. This temperature decrease is widely viewed as being critical for more widespread applications in fuel conversion to electricity (fuel cells) [58-60], electricity conversion to fuel (electrolysis) [61], electricity storage (reversible cells) [62, 63], and chemical processing (catalytic membrane reactors and oxygen generators) [62-66]. The cathode oxygen reduction reaction is usually the process limiting operating temperature reductions. Thus, there has been considerable activity on the discovery, study, development, and application of oxygen electrodes (cathodes) usually mixed ionically and electronically conducting (MIEC) oxide materials; the focus has been almost entirely on oxygen transport properties – oxygen diffusivity and vapor-solid oxygen exchange rate [67-70].

Achieving acceptable IT-SOC performance generally also requires modification of the electrode microstructure to achieve high active surface areas. To this end, nano-scale cathode morphology has been utilized in IT-SOC cathodes and have been successful in giving comparably high performance when operated at 500°C and below [6, 17]. Whilst these results represent a path

forward, it is of particular importance to explore how the performance of infiltrated materials evolves over time and much of the reported life testing has been limited to relatively short times (<500 h) compared to typical desired device lifetimes of >40,000 h. It is well known that nano-scale structures coarsen at elevated temperatures [71], and significant performance degradation is observed even under the short timescales reported in the literature [72]. In one study, the electrochemical performance degradation of $La_{0.6}Sr_{0.4}Co_{0.2}Fe_{0.8}O_3$ (LSCF) cathodes fabricated by wet-chemical impregnation (infiltration), a commonly-used method for producing nano-scale cathodes, was measured at temperatures higher than nominal operating temperatures in order to accelerate any degradation due to coarsening [35]. Unfortunately, both the amount of data and the testing time was limited (200–500 h), such that it was only possible to make approximate predictions regarding long-term degradation of these electrodes.

Evolution of the microstructure due to high temperature testing conditions can have a severe impact on long term degradation rates, rendering electrodes non-viable in long term operation. This is particularly true of infiltrated materials, which are comprised of materials with a relatively low melting point in comparison to the operating temperature of the cell. In order for them to be viable for commercial implementation, more information on their long term performance stability is necessary. As of the writing of this dissertation, there are relatively few studies that explore the long term performance of such materials [28, 34-36, 73-75].

In this study, the time- and temperature-dependent performance of a state-of-the-art nano-scale MIEC cathode – $Sm_{0.5}Sr_{0.5}CoO_3$ (SSC) infiltrated into a $Ce_{0.9}Gd_{0.1}O_2$ (GDC) scaffold is explored. Symmetric cells used in this study were subjected to accelerated degradation by aging

at temperatures between 650°C and 800°C for as long as 1500 h. The design of these experiments were to improve upon prior accelerated life tests by using more extensive lifetimes (1500 h) and repetition to ensure reproducibility of degradation behaviour under increasingly harsh coarsening conditions. Electrochemical impedance spectroscopy (EIS) measurements, carried out periodically during the life tests, were done in air at 600°C, a typical expected intermediate-temperature SOFC operating temperature. This produced an appropriate comparable condition for all tests, allowing long-term data to be fitted to a combined surface resistance and coarsening kinetics model. From this, a $t^{0.25}$ power law dependence was found, indicating that surface diffusion is the dominant mass transport pathway in SSC-GDC infiltrated cathodes. Scanning electron microscopy (SEM) was performed post-mortem to confirm the extent of coarsening of the MIEC nanoparticles. To simulate realistic degradation rates over cell lifetimes (40,000 h), long-term data were fitted to a combined surface resistance and coarsening kinetics model, and degradation rates were calculated over expected lifetimes. The model enables one of the first predictions of electrode stability over the 40,000 h times desired for SOC operation.

A large portion of the contents of this chapter have been published with significant contribution by Dr. Justin Railsback in refining the method of calculating degradation predictions [36]. Additionally, work by Dr. Megna Shah on LSCF infiltrated cathodes is referred to frequently as the direct predecessor to this work [23, 35].

6.1   Experimental Methods

Symmetric cell cathodes were used in this study to isolate cathodic degradation due to

nanoparticle coarsening. SSC-GDC cathode symmetric cells were prepared as described previously in Chapter 2. Cells of varying infiltration loading (7 vol%, 20 vol%, 30 vol%, 40 vol% SSC) were tested in order to determine the best infiltration loading for both short and long term performance. All loadings were aged at 650°C, 700°C, 750°C, and 800°C, but were periodically ramped down to 600°C for EIS testing in order to determine the performance of the cell at the target operating temperature at accelerated time points. Figure 6.1 illustrates graphically the testing process. Aging times that are given in this analysis do not include time spent at the target operating temperature. Such acceleration of degradation is successfully practiced in cases where device lifetimes are too long to allow extensive full-life tests, such as in integrated circuits [76].

Polarization resistances were measured as the difference between the real intercepts from Nyquist plots generated from EIS measurements. This data were then plotted against aging time and fitted to a combined surface resistance and coarsening theory model to both determine the resulting dependence on time and temperature, but also to predict the lifetime performance and behavior of these infiltrated samples.
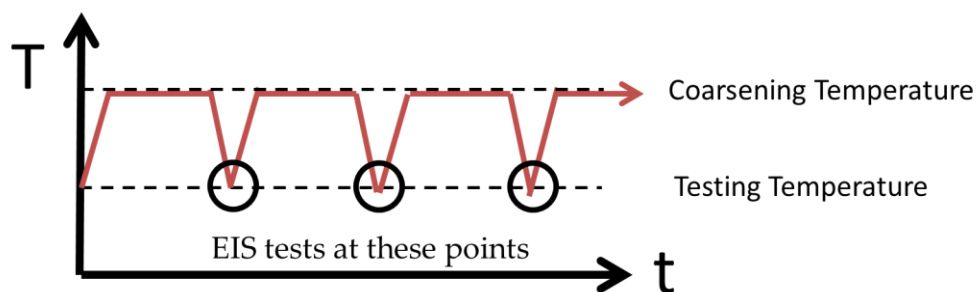
Figure 6.1: Graphical representation of testing regime for long term coarsening study. Cells are kept at an elevated temperature in comparison to the testing temperature in order to accelerate coarsening behavior and are periodically reduced in temperature to determine the performance at periodic time points.

Post-test analysis was done using either a Hitachi S-4800-II microscope or a Hitachi SU8030 microscope. Cells were fractured and the cross-section was examined for changes in microstructure from similar cells which experienced no thermal aging.

6.2   Experimental Results

6.2.1   Initial R_P Enhancement

Polarization resistance decreased between the initial and first time point, typically between 12 and 48 h. All time points afterward showed an increase in polarization resistance over time, as can be seen in Figure 6.2. The source of the decrease in polarization resistances at very short testing times is currently unknown, but has been observed in all SSC-GDC samples that have been tested as part of this thesis work, as well as in similar studies by Shah on LSCF-GDC infiltrated cathode systems [23].
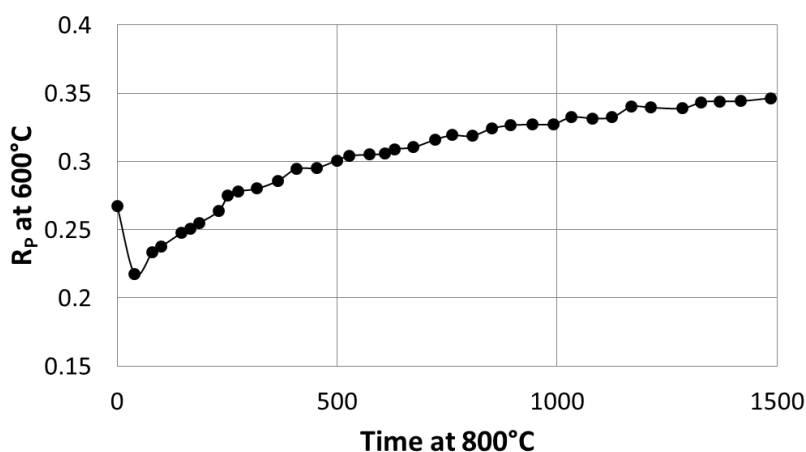
Figure 6.2: R_P vs. time. R_P values at t=0 are higher than subsequent time-points and not representative of the degradation trend observed over longer time periods.

It is possible that this initial change in performance is due to strontium surface enrichment, which is observed in strontium-containing cathode materials such as LSM, LSC, and LSCF during short operating times (< 100 h) [73, 77-83]. It is unknown what the effect of strontium segregating from the cathode material has on electrochemical performance. Most studies have seen a decrease in performance, however, in the case of some LSM report; polarization resistance was improved by strontium enrichment [84]. Several groups are currently studying this effect further [73, 78, 80-84].

What is most interesting about the performance enhancement we see in these samples is that it is only seen at times < 48 h before the onset of thermal degradation sets in. It is possible that this is a break-in mechanism that is similar to that which is seen in LSM cathodes [85, 86], however determination of the effect of this particular phenomenon is outside of the scope of this thesis work.

6.2.2 Power-Law Fit of Long Term Data

The evolution of R_P over time for SSC-GDC infiltrated symmetric cell cathodes was fit to a combined surface resistance and coarsening kinetics model,

$$(6.1) \qquad R_P = \sqrt{\frac{R_s}{\sigma_{ion} C_f}} \left(l_{C,0}^n + K_D t\right)^{1/2n} \coth\left(L\left(l_{C,0}^n + K_D t\right)^{-1/2n} \sqrt{\frac{C_f}{\sigma_{ion} R_s}}\right)$$

which is explained in further detail in Chapter 3 and in the literature [36]. Briefly, polarization resistance is related to the surface resistance of the infiltrated material and evolves based on

changes to the feature size via the relation $a = fC/l_C$, where C is the surface to volume shape factor ratio that depends on the geometry of the SSC infiltrate particles [87], typically ~6 for a hemispherical cap, and f is the SSC volume fraction. This model, developed by Dr. Railsback [36], is more accurate in predicting the behavior of infiltrated cathodes than previous models used [17, 23, 35], as will be described in further detail in Section 6.3.3 of this thesis. Cells of varying infiltration loading were coarsened at temperatures ranging from 650°C to 800°C. EIS testing for all cells was completed at 600°C and R_P determined by the difference between the real intercepts of the nyquist data and fit to this model.

In order to determine the value of n in Eqn 6.1 that best fits the experimental data, least squares analysis was used to evaluate the quality of the fits. An example of fits with different n values is shown in Figure 6.3. For most data sets it was only possible to obtain accurate fits over the entire range of infiltration loadings with n = 4. The results clearly show that n = 4 , a value expected if cation transport takes place via surface diffusion [48, 88], gives the best fits, in agreement with prior work on infiltrated LSCF cathodes [34, 35].
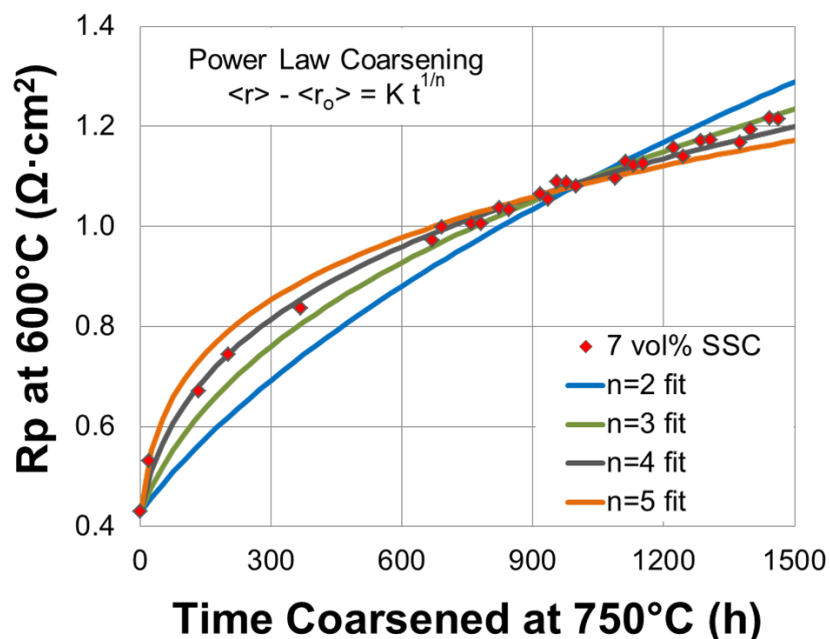
Figure 6.3: An example of best fits for modeling long term coarsening behavior. Fits were obtained via least-square fitting.

Figure 6.4, taken directly from [36], summarizes the results of electrochemical impedance spectroscopy (EIS) measurements carried out during life tests of five different but identically-prepared symmetric cells. The samples all showed the same initial value of R_P, within $\sim 10\%$, showing the good cell-to-cell reproducibility. As expected, each of the life tests shown in Fig. 6.3 shows an increase in R_P with time. At 800 °C, the initially fast resistance increase slows gradually during the life test. At lower temperatures, the rate of increase is less, and remains essentially constant throughout the test. Samples tested under identical conditions showed good agreement, with the exception of a noted slight offset of initial R_P values for samples degraded at 700°C. This offset did not affect the comparable rate at which the samples degraded.
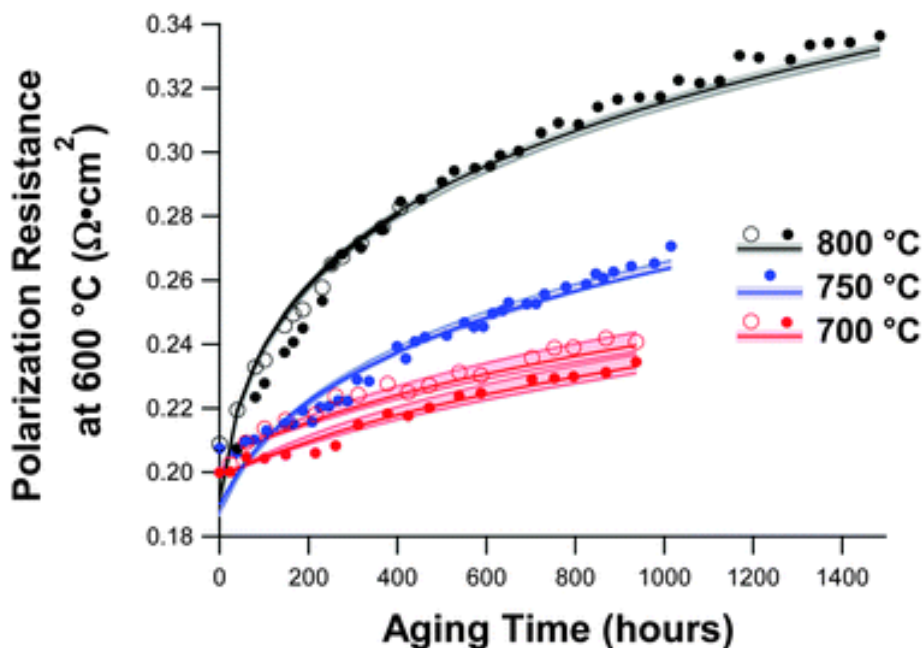
Figure 6.4: Cathode polarization resistance of SSC-infiltrated symmetric cells, taken from EIS data measured in air at 600 °C versus ageing time at various temperatures. Also shown are the overall best fits to the data using equation (6.1). The slight cell-to-cell variations in the initial resistance were modeled by assuming slight variations in the initial cathode. Note that the fits to the two 800°C aged cells were essentially identical, and so only one curve is visible. Solid curves indicate predictions using best fit values, while the broader shading indicates predictions for the range of $K_{D,0}$ and E_D values that provide good overall quality of fit. Figure taken directly from [36] with permission.

The results in Figure 6.3 can be explained by particle coarsening models that have been successfully applied to a range of materials, including catalyst nano-particles on oxide supports [33, 89, 90]. In the present model, only the SSC coarsening is considered, because it is primarily the SSC surface area that determines R_P. The GDC backbone presumably evolves much less than the SSC because of its larger particle size and higher melting point; furthermore, any changes are not expected to greatly impact the role that GDC plays in the electrode – oxygen ion transport between the electrolyte and the SSC.

Since the EIS measurements were always done at 600 °C, the values in Equation 6.1 that relate to electrode function were taken for this temperature, i.e., R_S(SSC) = 25 Ω cm^2 [17] and σ_{ion}(GDC) = 0.0024 S cm^{-1}. The latter value is an effective conductivity, taken to be less than the conductivity of sintered sub-micron GDC at 600 °C (0.007 S cm^{-1}) [91], accounting for a cathode GDC solid fraction of 0.46 and a tortuosity factor of 1.29 as determined by FIB-SEM [36]. The values of C, ~6, and f, ~0.2, were allowed to vary somewhat for each cell corresponding to sample-to-sample variations in SSC particle shape and volume fraction, respectively.

Equation 6.1 yields good fits to the time- and temperature-dependent polarization resistance data. Best fits were obtained with n = 4, a value expected if cation transport takes place via surface diffusion [48, 88]. Figure 6.4 shows the overall best fit to the data that was obtained with the values $l_{C,0}^n$ = 50 nm, E_D = 2.81 eV, and $K_{D,0}$ = 1.85 × 10^{-13} cm s^{-1}. In order to probe the quality of the fitting results, a range of $K_{D,0}$ and E_D values were used, up to a point where the quality of fit χ^2 value increased by 10% above the optimal fit value. This yielded fit values that ranged from E_D = 2.60 eV and $K_{D,0}$ = 1.77 × 10^{-14} cm s^{-1} at one extreme, to E_D = 2.92 eV and $K_{D,0}$ = 6.50 × 10^{-13} cm s^{-1} at the other. Fig. 6.4 shows the range of these fits as shaded regions.

6.2.3 Nano-particle Coarsening

Post-test analysis was completed on cells that were both not tested under accelerated degradation conditions and those that were completed as part of this study to confirm the extent of coarsening on infiltrated nano-particles. Coarsening of nano-scale SSC particles is readily observed after ageing at elevated temperatures, as demonstrated in Figure 6.5, which shows an

examples of SEM images taken from as-prepared SSC-infiltrated GDC scaffolds and after ageing at 800°C for 400 and 1471 h. To quantify this increase in particle size, measurements of particle diameters based on particles that were deposited at the electrode/electrolyte interface were averaged over a minimum of 15 infiltrated particles from at least 3 different regions along the interface. Analysis of the images indicates that the average size, $l_{C,0}^{n}$, was measured to be 50 nm initially, increased to 65 nm after 400 h and 173 nm after 1500 h ageing. Further information on the method used for determining $l_{C,0}^{n}$ can be found in Chapter 3.
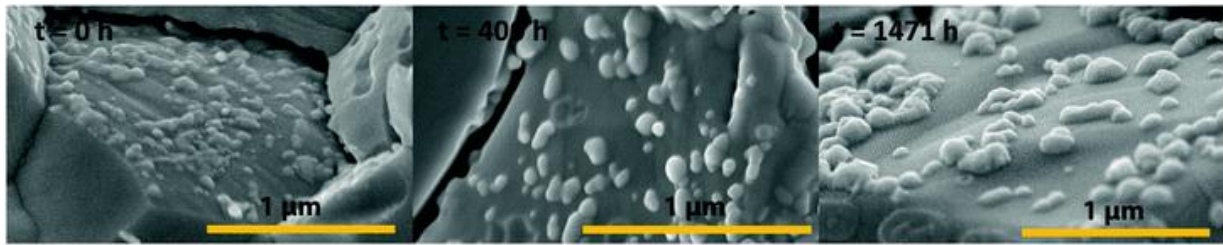
Figure 5.5: SEM images of $Sm_{0.5}Sr_{0.5}CoO_3$ (SSC) particles on Gd-doped Ceria (GDC) surfaces taken for ageing times t = 0 h (the as-prepared cathode), t = 400 h, and t = 1500 h at 800 °C. These images were taken at a flat portion of the GDC electrolyte at the electrode/electrolyte interface; this was done because it was not possible to resolve the SSC particles within the electrode via either contrast or size differences. Figure taken directly from [36] with permission.

While it was found that particle sizes increased with temperature and time, increasing by a factor of three from estimated initial particle sizes, $l_{C,0}^{n}$, for samples coarsened at 800°C for 1500 h, both initial and final average particle sizes were not consistent with particle sizes that were calculated via surface resistance model [17],

$$(6.2) \qquad\qquad Rp = \frac{Rs_{SSC}}{A_{SSC}/A_{FP}}$$

Here the polarization resistance is equal to the surface resistance of SSC, divided by the surface area of SSC normalized by the cathode footprint area. Initial R_P values suggested a much larger initial particle size than those that were measured via SEM image analysis. Approximately 550 nm in diameter was predicted using the surface resistance model for initial particle sizes as opposed to the 50 nm particle sizes expected from the infiltration particle size analysis presented in Chapter 3. Final particle sizes were estimated to be 785 nm in diameter in comparison to the measured particle size of 173 nm that was measured via SEM image analysis.

It was possible that these exaggerated particle sizes were partially due to fact that the surface resistance model used in the coarsening model to estimate polarization resistance does not take into account any losses associated with the microstructure of the cathode or the material used for the scaffold, so the expected value of $l_{C,0}^n$ was recalculated using the SIMPLE model, which accounts for polarization loss due to both the surface resistance of the infiltrate material and ionic transport through the ion-conducting scaffold material [17].

(6.3)
$$Rp = \frac{r\left(\frac{R_S A_{Sc}}{A_{Inf}}\right)}{\left(\frac{1+\beta}{1+\beta\,\exp\left(\frac{-2h}{\alpha}\right)}\right)r(1-p)\exp\left(\frac{-h}{\alpha}\right)+\frac{\left(1+\beta\,\exp\left(\frac{-h}{\alpha}\right)\right)}{\left(1+\beta\,\exp\left(\frac{-2h}{\alpha}\right)\right)}\alpha\left(1-\exp\left(\frac{-h}{\alpha}\right)\right)+pr}$$

Where

(6.4)
$$\alpha = \sqrt{\sigma_{V_{O,Sc}^{\cdot\cdot}}\, r(1-p)\frac{R_S A_{Sc}}{A_{Inf}}}$$

$$(6.5) \qquad \beta = \frac{\sigma_{V_{O,Sc}^{\bullet\bullet}} \frac{R_S A_{Sc}}{A_{Inf}} - \alpha}{\sigma_{V_{O,Sc}^{\bullet\bullet}} \frac{R_S A_{Sc}}{A_{Inf}} + \alpha}$$

The underlying factors are explained in further detail in Chapter 3 and in the literature [17, 18, 23, 34]. Values of r, denoting the initial particle size in this model, which were calculated using the SIMPLE model were lower than those calculated using the SR model, but were not quite as low as those observed in SEM images. Values of 210 nm initial particle size and 400 nm final particle size were calculated using this method. Calculations using the improved Equation 6.1, which utilizes the transmission line model, does a much better job of calculating this discrepancy, by producing an initial particle size of 70 nm and a final particle size of 156 nm [36].

A second look at how nanoparticles are represented in all of these equations leads us to the understanding that the representation of the infiltrate geometry and how it interacts with the scaffold must be as accurate as possible and over-simplification will lead to significant errors. For each of these calculations it is assumed that the volume of SSC infiltrated onto the GDC scaffold material is made of discrete hemispherical nanoparticles and that the entire surface area of these hemispheres is active. It is more likely, particularly for samples with high infiltration loading, that these nanoparticles are not discrete, but rather overlapping to produce non-hemispherical agglomerates with reduced surface area. In this case, the effective nanoparticle size would be much larger because the active surface area represented is lower than that of the discrete hemisphere nanoparticle case. A schematic representing this geometry can be seen in Figure 6.6. This hypothesis is also supported by the increase in R_P value for 30 vol% SSC samples over their

20 vol% SSC counterparts, as seen in Figure 6.7 (taken directly from [36]).
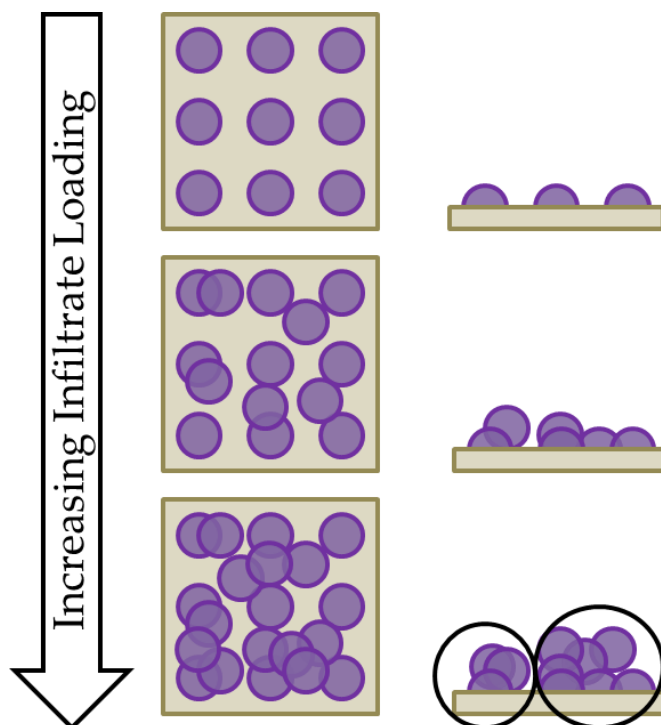
Figure 6.6: Schematic illustrating how nanoparticles can agglomerate and have geometries that are non-representative of hemispherical particles.

What this means is that as infiltration loading increases, it will appear that degradation rates will decrease when in fact the effective value of the initial particle size has increased and these larger effective particles will coarsen at a slower rate than their smaller, more isolated counterparts. High infiltration loading not only decreases polarization resistance by increasing active surface area for the ORR reaction, but it also increases the effective feature size, which leads to cells with higher stability and lower degradation rates.
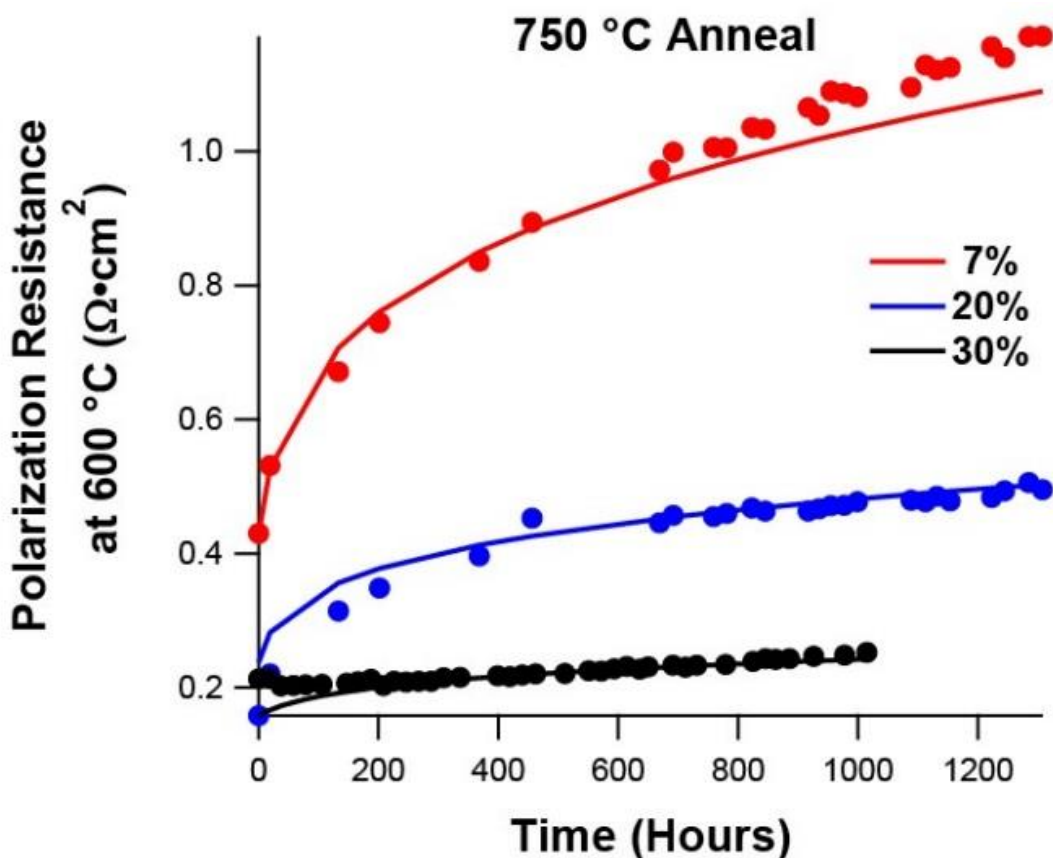
Figure 6.7: Cathode polarization resistance of SSC-infiltrated symmetric cells with varying SSC volume fractions f, taken from EIS data measured in air at 600°C, versus ageing time at 750°C. Also shown are the overall best fits to the data using Equation 6.1. Figure taken directly from [36] with permission.

It should be noted that different degradation rates were obtained for samples of varying loading, as can be seen in Figure 6.7. This effect has not been previously reported in the literature. Initial particle size was estimated to be the same for all samples, as reported in Chapter 3, regardless of infiltration loading, which contradicts the performance expected based on the model. Further analysis of the data showed that for samples with high infiltration loading (> 30 vol % infiltrate), there was an increase in initial polarization resistance that was inconsistent with

estimations on the approximate active surface area of SSC nanoparticles available for the oxygen reduction reaction.

Based on the expected trends resolved from the coarsening model and assuming that SSC feature size does not increase with loading, the value of R_{P0} is expected to decrease with increased loading due to higher SSC surface area, but the rate of coarsening at a given temperature should be the same. Instead it was observed that the degradation rate decreased with increasing loading, as can be seen most clearly in Figure 6.6.

6.3   Conclusions

SSC-GDC symmetric cell cathodes were subjected to accelerated degradation by aging at temperatures between 650°C and 800°C for as long as 1500 h. Microstructural and electrochemical degradation of infiltrated SSC-GDC cathodes is observed and fitted to a combined surface resistance and coarsening kinetics model and a $t^{0.25}$ power law dependence was found, indicating that surface diffusion is the dominant mass transport pathway in SSC-GDC infiltrated cathodes. From this, a coarsening model is presented that accurately fits the data, as well as previously reported accelerated life test data for infiltrated LSCF-GDC cathodes.

The data presented shows that infiltrated cathodes appear to have an inverse dependence on infiltrate loading, however, this loading dependence is associated with effective initial particle size. Low loading samples may exhibit unusually large degradation rates, as infiltrate particles may become isolated, and therefore inactive, over time. High loading samples will have non-representative nano-particle sizes due to overlapping particles at t_0, causing the effective feature

size to be high. This is supported by an observed increase in R_P in high loading samples, suggesting a decrease in active surface area over cells with lower infiltrate loading. Results suggest that degradation due to thermal conditioning is both reproducible and predictable.

6.4   Acknowledgements

Chapter 7

Long Term Performance Predictions of $Sr_{0.5}Sm_{0.5}CoO_{3-\delta}$ Infiltrated Cathodes

Infiltrated cathodes have been shown to yield low polarization resistances during intermediate temperature operation [6, 8, 12, 92]. While the initial performance of these cells is quite promising, long term behavior of these nano-composite materials need to be understood in order for these cathode systems to be viable in commercial devices. Long expected SOFC lifetimes (>40,000 h) require that degradation losses be small, around the order of 0.2 % / kh [19].

Work reported in Chapter 6 of this thesis on SSC-GDC infiltrated electrodes, as well as previous work by Shah on $La_{0.6}Sr_{0.4}Co_{0.2}Fe_{0.8}O_{2.7}$ (LSCF) infiltrated GDC electrodes determined the extent of cell degradation for infiltrated cathodes due to particle coarsening[34, 35]. By annealing at elevated temperatures, between 650°C and 850°C, and confirming particle evolution fits that were expected from coarsening theory, particle size fits were then extrapolated for long testing times and used to predict R_P. Fitting parameters obtained through accelerated coarsening experiments were used to calculate the expected degradation of infiltrated cathodes when tested over the expected lifetime of an SOFC system. Material dependent fitting parameters were experimentally determined, allowing for calculated predictions of electrodes with varying microstructure parameters to be explored without necessitating time intensive experimentation.

In this study, results from electrochemical performance degradation studies discussed in Chapter 6 are used to predict cell operating conditions where required performance and long term stability are both achieved. In addition, a new electrode material figure of merit based on both performance and stability metrics is proposed. An implication of this study is that cation diffusion,

which determines the coarsening rate, must be considered in concert with oxygen transport kinetics in the selection of electrode materials to achieve the high performance and stability required. The model enables one of the first predictions of electrode stability over the ~40,000 h times desired for SOC operation, and shows that there are clear limits on the starting MIEC particle sizes, operating temperatures, and polarization resistance values that can be achieved while maintaining acceptable stability.

7.1   Lifetime Performance Prediction of Infiltrated Cathodes

The model used in Chapter 6 can also be used to make predictions of expected cathode performance for extended times under various conditions. Substituting the operating temperature in lieu of the coarsening temperature in our combined surface resistance and coarsening theory model,

$$(7.1) \qquad R_P = \sqrt{\frac{R_s}{\sigma_{ion}Cf}}\,(l_{C,0}^n + K_D t)^{1/2n} \coth\left(L\left(l_{C,0}^n + K_D t\right)^{-1/2n}\sqrt{\frac{Cf}{\sigma_{ion}R_s}}\right),$$

and evaluating over the expected lifetime of a SOFC device provides the expected degradation curve for infiltrated cathodes due to nano-particle coarsening. Unlike Figure 6.4 where the cell is maintained at higher temperatures to accelerate degradation but the resistance is measured at 600°C, Figure 7.1, taken directly from [36], shows an example where SSC particle sizes are varied in order to the predict R_P versus time for a cell operated at 600°C. The ranges, shown as shaded regions, indicate the variability in the predicted values based on acceptable fitting ranges calculated in Chapter 6. It is seen that reducing the initial size below 50 nm yields a substantial

decrease in initial R_P, well below the 0.2 Ω cm^2 target, but coarsening is much faster, resulting in rapid particle size and R_P increases in the first 10,000 h. In fact, it is seen that regardless of starting particle size below 50 nm, particle size and R_P values are nearly the same after 10,000 h operation.
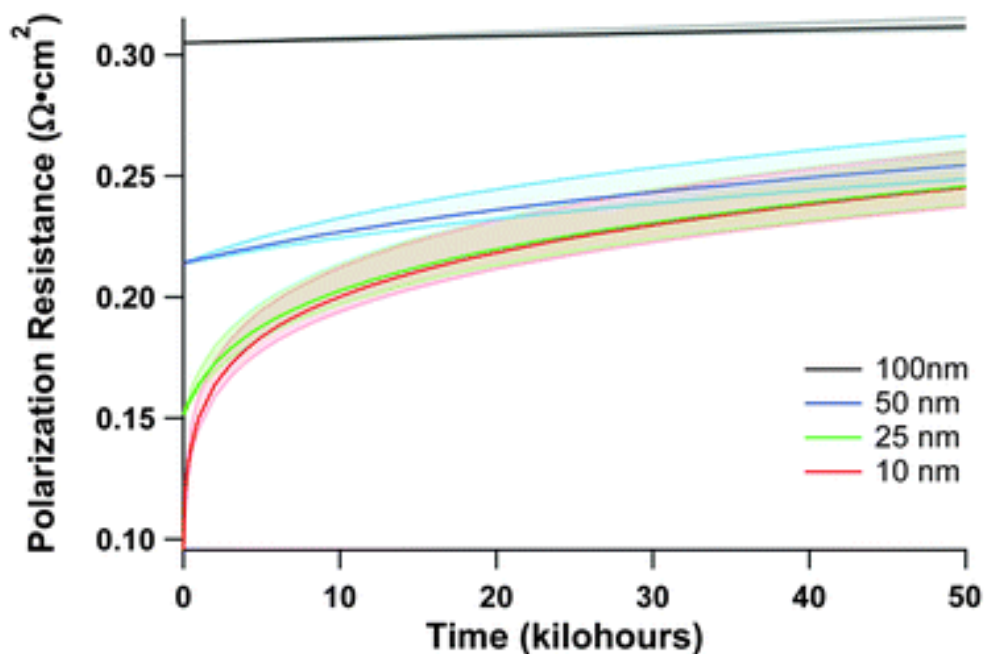
Figure 7.1: Predicted polarization resistance versus time for cathodes with initial SSC particle sizes of 10, 25, 50, and 100 nm, operated at a temperature of 600 °C. Solid curves indicate predictions using best fit values while the broader shading indicates predictions for the range of $K_{D,0}$ and E_D values that provide good overall quality of fit. Figure taken directly from [36] with permission.

These observations suggest dual criteria for infiltrated cathodes. A balance between the value of R_P, which should be less than some acceptable value, e.g., 0.1 or 0.2 Ω cm^2, and the degradation rate, which should be less than an acceptable value, e.g., 0.2 or 0.5% resistance increase per kh of operation.

Figure 7.2 , taken directly from [36], illustrates a combined plot of these criteria with both

the less stringent 0.5% per kh degradation requirements related to the U.S. Department of Energy 2015 targets for stationary power and a more stringent requirement of 0.2% per kh, which is stricter than the 2020 targets of 0.3% per kh [19]. The aqua and blue curves indicate the boundary where initial particle size generates a degradation rate is 0.2% per kh or 0.5% per kh over 50,000 h respectively, versus operating temperature and values above these boundaries will produce lower degradation rates. The red and pink curves denote the boundary where initial particle sizes produce initial R_P values of 0.2 Ω cm^2 and 0.1 Ω cm^2 respectively, versus operating temperature. Particle sizes below these boundaries will produce even lower values of R_P. Cathodes must satisfy both criteria outlined, as indicated by the shaded region in Figure 7.2, and therefore electrodes will need both have the appropriate initial particle size and be operated within the range of temperatures shown to have acceptable degradation rates. For an infiltrated SSC-GDC electrodes, this relates to a minimum operating temperature of 590 °C, corresponding to a starting particle size of 40 nm for the least stringent requirements. For the lower resistance and degradation rate targets, the minimum operating temperature is 670 °C, corresponding to an initial size of 100 nm.
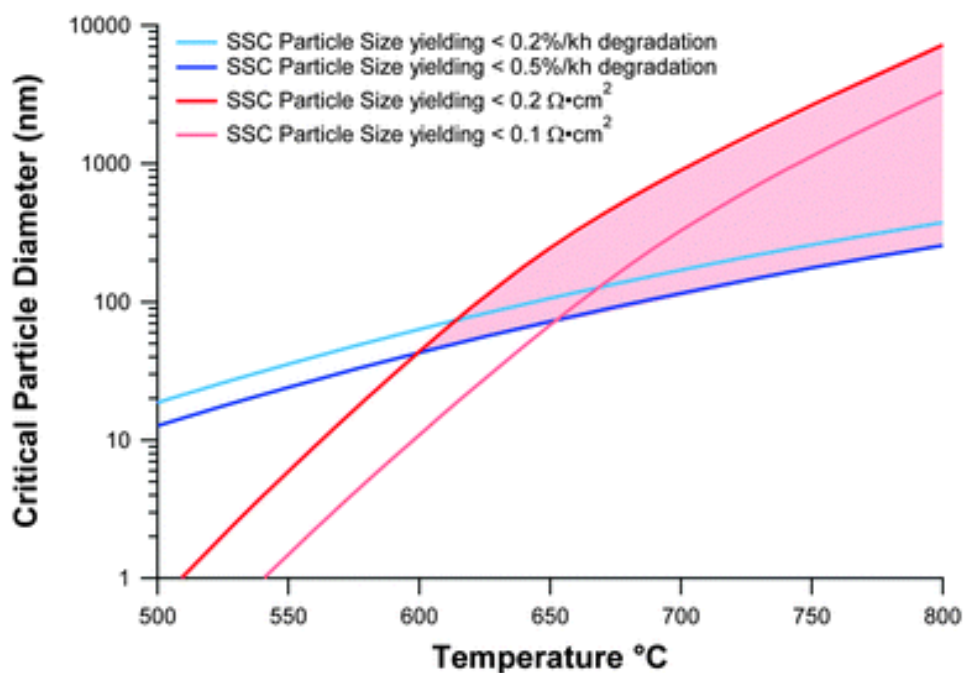
Figure 7.2: A plot of critical SSC particle diameters that provide target performance and stability values, versus cell operating temperature. The red and pink curves show the diameter yielding target cathode resistance values of R_P = 0.2 or 0.1 Ω cm2. The aqua and blue curves show the diameter yielding target degradation rate. The shaded area shows the SSC particle sizes and cell operating temperatures that yield the desired stability and performance; for clarity, the shading is shown only for the target values $R_P \leq 0.2$ Ω cm^2 and $\leq 0.5\%$ per kh. Figure taken directly from [36] with permission.

The same analysis was completed on LSCF-GDC data collected by Shah [REF] using the applicable material values for LSCF and GDC. The results can be seen in Figure 7.3, where the curves again have similar meaning, and show that the higher surface resistance for LSCF (28.5 Ω cm^2 at 600°C versus 25 Ω cm^2 for SSC) and different K_D and E_D values (see Table A2) significantly narrows the range of usefulness for LSCF compared to SSC. Minimum operating temperature is achieved with the less stringent degradation rate of 0.5% per kh at 595°C, corresponding to an initial particle size of 40 nm.
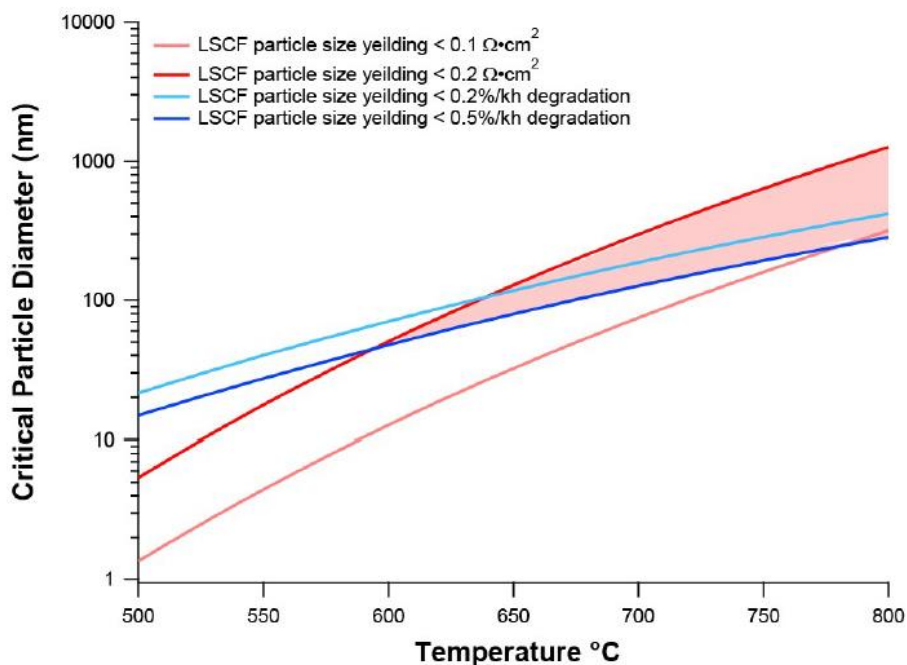
Figure 7.3: A plot of critical LSCF particle diameters that provide target performance and stability values, versus cell operating temperature. The red and pink curves show the diameter yielding target cathode resistance values of $R_P = 0.2$ or 0.1 Ω cm^2. The aqua and blue curves show the diameter yielding target degradation rate. The shaded area shows the LSCF particle sizes and cell operating temperatures that yield the desired stability and performance; for clarity, the shading is shown only for the target values $R_P \leq 0.2$ Ω cm^2 and $\leq 0.5\%$ per kh. Figure taken directly from [36] with permission.

The results for SSC and LSCF cathodes illustrate the behaviour of coarsening processes in this class of materials and it seems likely that other compositions consisting of an MIEC infiltrated into an ionically-conducting scaffold will exhibit qualitatively similar behaviour, however the quantitative predictions described above are only valid for the infiltrated material system they represent. Structural differences between different cathodes can be expected to affect long-term degradation behavior, as this model does not take into account complex interactions where, for

example, multiple infiltrate materials or coatings are implemented [81, 93]. Nonetheless, coarsening processes which are inherent in high temperature SOC systems will ultimately limit the degree to which particle size and operating temperature can be decreased. Identification of materials with suitably high low cation diffusion and high oxygen transport and surface resistance will be necessary to produce reliable next generation SOC electrodes.

It should be noted that this study focused on coarsening as the source of cathode degradation, however other mechanisms may also play a role in cathode degradation. For example, possible loss of electronic percolation during coarsening is not explored and may be a significant contributor of degradation if the amount of infiltration material is not sufficient to maintain electrical connectivity. Additionally, Sr segregation has been observed to degrade MIEC electrode performance over time [77-79]. For this particular study it is observed that increases in R_P correlate quantitatively with increases in SSC particle size, which provides strong evidence that coarsening is the primary mechanism here, but does not rule out the possibility for other Sr containing MIEC materials. Furthermore, the present results show that coarsening is fast, and hence is likely to be the dominant degradation mechanism. Results from both SSC and LSCF studies suggest that this will be the case for other MIEC electrodes with sufficiently small particle sizes. For larger particle sizes, such as those in conventionally produced SOFC electrodes, coarsening is expected to be very slow such that other degradation mechanisms may become dominant.

7.2   Conclusions

Fitting parameters extracted from accelerated coarsening tests were used in a combined surface resistance and coarsening theory model to calculate expected degradation behavior over SOFC device lifetimes (> 40,000 h) with varying operating temperatures and initial infiltrate feature sizes. These results represent the first example of SOFC cathode data and modeling leading to quantitative long-term stability predictions and demonstrate qualitative trends which have a critical implication for the development of SOC electrodes. Long-term stability, particularly coarsening kinetics, must be considered in concert with oxygen transport properties to select optimal cathode materials which can meet target performance criteria. Equation 7.1 shows that electrode resistance depends not only on materials constants, such as surface resistance R_S and oxygen conductivity σ_{ion}, but also on the initial particle size of the MIEC as it relates to the active surface area. As shown by the present results, the initial particle size has important implications on long-term stability. This leads to the unintuitive possibility of a material with inferior R_S and σ_{ion} producing superior performance if it is characterized by slower coarsening kinetics. Experimental and theoretical studies of cathode materials have largely ignored coarsening kinetics in favour on focusing on producing low initial values of R_P by prioritizing oxygen transport properties [67-70]. This approach could miss useful materials with improved stability or promote non-viable materials.

7.3   Acknowledgements

Chapter 8

Conclusions

This dissertation presents several studies on the electrochemical processes and stability of nano-scale infiltrated cathodes. Advancement of our understanding of these high-performance cathodes, particularly their rate limiting behavior under operating conditions and their microstructural stability under long testing times, can allow for future iterative improvements though rational design of these microstructures.

In this study, symmetric cell cathodes were prepared via wet infiltration of $Sr_{0.5}Sm_{0.5}CoO_3$ (SSC) nano-particles or $La_{0.6}Sr_{0.4}Co_{0.2}Fe_{0.8}O_{3-\delta}$ (LSCF) nano-particles via a nitrate process into porous $Ce_{0.9}Gd_{0.1}O_{1.95}$ (GDC) scaffolds, to be used as model systems to investigate performance and structural evolution. Detailed analysis of the cells was carried out using electrochemical impedance spectroscopy (EIS). Initial polarization resistances (R_P) as low as 0.11 $\Omega\,cm^2$ at 600ºC were obtained for these SSC-GDC cathodes, making them an ideal candidate for studying high-performance nano-structured electrodes.

The present results show that the infiltrated cathode microstructure has a direct impact on the initial performance of the cell. Small initial particle sizes and high infiltration loadings (up to 30 vol% SSC) improved initial R_P. A simple microstructure-based electrochemical model successfully explained these trends in R_P. Limitations of this model were due to the necessity of having accurate values of materials properties. Infiltration loadings below 5 vol% exhibited large polarization losses due to isolated and inactive particles. Infiltration loadings past 30 vol% exhibited a slight increase in initial R_P, indicating that SSC particles were overlapping, causing the

active surface area available for the oxygen reduction reaction to decrease with additional infiltrations. This, in turn, can lead to inaccurate estimations of $l_{C,0}^n$ as infiltrated particles can no longer be modelled accurately as hemispherical in shape based on SEM measurements of particle diameters.

Inaccuracies in the values of surface resistance, ionic conductivity, and infiltrate particle size can lead to predictions that are not representative of the system being tested. For models such as the simple infiltrated microstructure polarization loss estimation (SIMPLE) model to be useful, accurate microstructural parameters and materials properties need to be obtained for the system being modelled.

Further understanding of electrode performance was gleaned from fitting EIS data gathered under varying temperatures and oxygen partial pressures to equivalent circuit models. Both (RQ) and Gerischer impedance elements provided good fits to the main response in the EIS data, which were associated with the combination of oxygen surface exchange and oxygen diffusion in the electrode. Activation energies for this response was ~0.64 eV and 0.84 eV for 15 and 20 vol% SSC loadings respectively, irrespective of the model used. A gas diffusion response was also observed at relatively low pO_2, which while still small, was observable in the impedance data at 20% O_2 and identified in analysis of differences in impedance spectra (ADIS) analysis at 50% O_2.

The cells were subjected to life testing at temperatures between 650°C and 800°C for as long as 1500 h. EIS measurements, carried out periodically during the life tests, were done in air at 600°C, a typical expected intermediate-temperature SOFC operating temperature. These were accelerated tests because the annealing temperatures > 600ºC will accelerate temperature

dependent degradation processes such as nano-particle coarsening. Long-term R_P versus time data were fitted to a combined surface resistance and coarsening kinetics model, and a $t^{0.25}$ power law coarsening model was found to provide the best fits to the data, suggesting that surface diffusion is the dominant mass transport pathway in SSC-GDC infiltrated cathodes. That is, cathode degradation was due primarily to the coarsening-induced decrease in active SSC surface area. SEM performed after electrochemical life testing confirmed the extent of coarsening of the SSC nanoparticles. Results suggest that degradation due to thermal conditioning is both reproducible and predictable. From this, a coarsening model is presented that accurately fits the data, as well as previously reported accelerated life test data for infiltrated LSCF-GDC cathodes.

Low loading samples may exhibit unusually large degradation rates, as infiltrate particles may become isolated, and therefore inactive, over time. An important new finding is that increasing infiltration loadings yields a marked decrease in the long term degradation rate. It is noted, however, that increases in infiltration loading past 30 vol% may lead to a slight increase in R_P. High loading samples will have non-representative nano-particle sizes due to overlapping particles at t_0, causing the effective feature size to be high. This is supported by an observed increase in R_P in high loading samples, suggesting a decrease in active surface area over cells with lower infiltrate loading

The combined surface resistance and coarsening kinetics model was used to make predictions regarding long-term stability of infiltrated SSC electrodes. For an infiltrated SSC-GDC electrodes, a minimum operating temperature is 670 °C, corresponding to an initial size of 100 nm was necessary to meet the U.S. Department of Energy 2015 target for stationary power

requirement of 0.5% per kh degradation rate. These values were also calculated for a similar perovskite MIEC electrode, LSCF, using previously published values, resulting in a minimum operating temperature of 595°C, corresponding to an initial particle size of 40 nm to achieve a degradation rate of 0.5% per kh. The results for SSC and LSCF cathodes illustrate the behaviour of coarsening processes in this class of materials and it seems likely that other compositions consisting of an MIEC infiltrated into an ionically-conducting scaffold will exhibit qualitatively similar behaviour.

Chapter 9

Future Work

Extended Degradation Tests

While the accelerated coarsening tests covered over the course of this thesis work provide values for the approximate degradation rate of infiltrated nano-composite electrodes expected due to nano-particle coarsening, there is not an available data set of an infiltrated cathode tested for extended into testing times (> 10,000 h) at operating temperature with which to compare these values. Proof-of-concept work would be advantageous to both verify our fits and also determine if additional fitting parameters need to be included in our fitting models.

Full Cell Testing/DC Bias condition

Additional degradation mechanisms can arise from full cell tests or tests utilizing a DC bias. It has been seen that an increase in strontium segregation in LSM takes place under an applied bias, causing a decrease in R_P due to a surface that is more active to the oxygen reduction reaction [75, 83, 86, 94-96]. In other instances, applied bias may slow down the degradation rate. Harrison suggests that an imbalance in the surface charge in perovskite materials may lead to surface segregation [81]. Applied bias may offset or accelerate this process if this is indeed the source.

Previous work has also found that some materials, such as silver, migrate under applied load [97-99]. While this is a degradation mechanism that should be avoided, it is not inherently associated with the cathode, but rather a degradation mechanism that is associated with the choices of current collect and sealing materials. It does, however, illustrate that applied bias can have

unintended effects on the materials utilized in the cell. Further work to understand how cathode materials behave under these conditions will be necessary to determine if chemical instability under load causes changes in performance.

Decreased Degradation Rate Due to Surface Modification

As shown in Chapter 2, in order to have an acceptably low initial polarization resistance at intermediate operating temperatures, initial particle sizes $l_{C,0}^n$ for infiltrated materials need to be sufficiently small. However, the driving force for coarsening is much higher for small particles and any initial performance benefit that is achieved by reducing the value of $l_{C,0}^n$ could be lost within the first several hundred hours, leading to much higher lifetime degradation rates.

In order to balance the need for low R_{P0} values and the requirement of low degradation rates, on the order of 0.2%/kh over a lifetime of ~40,000 h for cathodes, a number of actions can be taken. One is to use a material with lower surface exchange resistance. Another is to increase the infiltration loading so that the value of $l_{C,0}^n$ is effectively larger. Additionally, a material with slower coarsening kinetics could be used. While each of these options are possible, they may not necessarily be easy or cost-effective to determine experimentally.

Previous work by Shah showed a decrease in the degradation rate of LSCF-GDC infiltrated cells over the course of 100 h when GDC was also infiltrated into the cathode [34]. It appeared that the addition of GDC nano-particles acted as a coarsening inhibitor between LSCF particles, but this conclusion has not been verified. Additions of a second phase via infiltration or ALD deposition may slow the coarsening kinetics of infiltrated nano-particles.

Work by Gong et al suggested that a nanoscale layer of ZrO_2 deposited via atomic layer deposition (ALD) lends a dramatic reduction in degradation rate for infiltrated cathodes made of LSCo-GDC [73, 92]. This decrease of degradation rate was also, surprisingly, accompanied by a decrease in R_P. Work done by Yu et al suggests that non-continuous coverage will give enhanced performance, while complete coverage of material may act as an insulating later [94].

It is difficult to tell at this stage what role ALD modification will play. Further work to characterize not only the surface composition and evolution of active surface area, but also in the surface kinetics of enriched/modified surfaces will need to be completed.

References

1. Hosoi, K., M. Ito, and M. Fukae, *Status of National Project for SOFC Development in Japan.* Solid Oxide Fuel Cells 12 (Sofc Xii), 2011. **35**(1): p. 11-18.

2. O'Hayre, R.P., *Fuel cell fundamentals*. 2nd ed. 2009, Hoboken, N.J.: John Wiley & Sons. xxv, 546 p., 4 p. of plates.

3. Bedringas, K.W., et al., *Energy analysis of solid-oxide fuel-cell (SOFC) systems.* Energy, 1997. **22**(4): p. 403-412.

4. Singhal, S.C. and K. Kendall, *High temperature solid oxide fuel cells : fundamentals, design, and applications*. 2003, Oxford ; New York: Elsevier. xvi, 405 p.

5. Chan, S.H., C.F. Low, and O.L. Ding, *Energy and exergy analysis of simple solid-oxide fuel-cell power systems.* Journal of Power Sources, 2002. **103**(2): p. 188-200.

6. Ding, D., et al., *Enhancing SOFC cathode performance by surface modification through infiltration.* Energy & Environmental Science, 2014. **7**(2): p. 552-575.

7. Sun, C., R. Hui, and J. Roller, *Cathode materials for solid oxide fuel cells: a review.* Journal of Solid State Electrochemistry, 2009. **14**(7): p. 1125-1144.

8. Vohs, J.M. and R.J. Gorte, *High-Performance SOFC Cathodes Prepared by Infiltration.* Advanced Materials, 2009. **21**(9): p. 943-956.

9. Yeh, T.C., J.L. Routbort, and T.O. Mason, *Oxygen transport and surface exchange properties of Sr0.5Sm0.5CoO3-delta.* Solid State Ionics, 2013. **232**: p. 138-143.

10. Xiong, H., et al., *Low-temperature electrochemical characterization of dense ultra-thin lanthanum strontium cobalt ferrite (La0.6Sr0.4Co0.8Fe0.2O3) cathodes synthesized by RF-sputtering on nanoporous alumina-supported Y-doped zirconia membranes.* Journal of Power Sources, 2009. **193**(2): p. 589-592.

11. Baumann, F.S., et al., *Quantitative comparison of mixed conducting SOFC cathode materials by means of thin film model electrodes.* Journal of The Electrochemical Society, 2007. **154**(9): p. B931-B941.

12. Jiang, S.P., *A review of wet impregnation - An alternative method for the fabrication of high performance and nano-structured electrodes of solid oxide fuel cells.* Materials Science and Engineering a-Structural Materials Properties Microstructure and Processing, 2006. **418**(1-2): p. 199-210.

13.   Jiang, Z., C. Xia, and F. Chen, *Nano-structured composite cathodes for intermediate-temperature solid oxide fuel cells via an infiltration/impregnation technique.* Electrochimica Acta, 2010. **55**(11): p. 3595-3605.

14.   Sun, C.W., R. Hui, and J. Roller, *Cathode materials for solid oxide fuel cells: a review.* Journal of Solid State Electrochemistry, 2010. **14**(7): p. 1125-1144.

15.   Abdel-Salam, A.S.G., J.B. Birch, and W.A. Jensen, *A Semiparametric Mixed Model Approach to Phase I Profile Monitoring.* Quality and Reliability Engineering International, 2013. **29**(4): p. 555-569.

16.   Zhao, F., et al., *Novel nano-network cathodes for solid oxide fuel cells.* Journal of Power Sources, 2008. **185**(1): p. 13-18.

17.   Nicholas, J.D., et al., *Use of the Simple Infiltrated Microstructure Polarization Loss Estimation (SIMPLE) model to describe the performance of nano-composite solid oxide fuel cell cathodes.* Physical Chemistry Chemical Physics, 2012. **14**(44): p. 15379-15392.

18.   Nicholas, J.D. and S.A. Barnett, *Measurements and Modeling of Sm0.5Sr0.5CoO3-x-Ce0.9Gd0.1O1.95 SOFC Cathodes Produced Using Infiltrate Solution Additives.* Journal of The Electrochemical Society, 2010. **157**(4): p. B536-B541.

19.   U.S. Department of Energy, 2014.

20.   White, B., *DOE Solid Oxide Fuel Cell Program Status*. 2012.

21.   Office of Fossil Energy, F.C.P., *FY 2010 Annual Report.* 2010.

22.   Adler, S.B., *Limitations of charge-transfer models for mixed-conducting oxygen electrodes.* Solid State Ionics, 2000. **135**(1-4): p. 603-612.

23.   Shah, M., J.D. Nicholas, and S.A. Barnett, *Prediction of infiltrated solid oxide fuel cell cathode polarization resistance.* Electrochemistry Communications, 2009. **11**(1): p. 2-5.

24.   Kungas, R., et al., *Understanding Surface Reactions in SOFC Cathodes Prepared by Infiltration.* Ionic and Mixed Conducting Ceramics 8, 2012. **45**(1): p. 275-284.

25.   Armstrong, T.J. and J.G. Rich, *Anode-supported solid oxide fuel cells with La0.6Sr0.4CoO3-lambda-Zr0.84Y0.16O2-delta composite cathodes fabricated by an infiltration method.* Journal of The Electrochemical Society, 2006. **153**(3): p. A515-A520.

26.   He, H.P., et al., *Low-temperature fabrication of oxide composites for solid-oxide fuel cells.* Journal of the American Ceramic Society, 2004. **87**(3): p. 331-336.

27.   Huang, Y.Y., et al., *Characterization of Sr-doped LaCoO3-YSZ composites prepared by impregnation methods.* Journal of The Electrochemical Society, 2004. **151**(10): p. A1592-A1597.

28.   Sholklapper, T.Z., et al., *Synthesis and stability of a nanoparticle-infiltrated solid oxide fuel cell electrode.* Electrochemical and Solid State Letters, 2007. **10**(4): p. B74-B76.

29.   Nicholas, J.D. and S.A. Barnett, *Effect of Infiltrate Solution Additives on Samarium Strontium Cobaltite - Cerium Gadolinium Oxide Nano-Composite SOFC Cathodes.* Solid Oxide Fuel Cells 11 (Sofc-Xi), 2009. **25**(2): p. 2435-2442.

30.   Kungas, R., I. Kivi, and E. Lust, *Effect of Cell Geometry on the Electrochemical Parameters of Solid Oxide Fuel Cell Cathodes.* Journal of The Electrochemical Society, 2009. **156**(3): p. B345-B352.

31.   Okawa, Y., et al., *Thermal stability of nanometer-sized NiO and Sm-doped ceria powders.* Journal of Materials Research, 2002. **17**(9): p. 2266-2274.

32.   Ahn, T.M., P. Wynblatt, and J.K. Tien, *Coarsening Kinetics of Platinum Particles on Oxide Substrates.* Acta Metallurgica, 1981. **29**(5): p. 921-929.

33.   Wynblatt, P. and N.A. Gjostein, *Model Study of Catalyst Particle Coarsening.* Scripta Metallurgica, 1973. **7**(9): p. 969-975.

34.   Shah, M., *An Experimental and Computational Study of Solid Oxide Fuel Cell Electrodes*, in *Materials Science and Engineering*. 2011, Northwestern University: Evanston, IL.

35.   Shah, M., P.W. Voorhees, and S.A. Barnett, *Time-dependent performance changes in LSCF-infiltrated SOFC cathodes: The role of nano-particle coarsening.* Solid State Ionics, 2011. **187**(1): p. 64-67.

36.   Call, A.V., et al., *Degradation of nano-scale cathodes: a new paradigm for selecting low-temperature solid oxide cell materials.* Physical Chemistry Chemical Physics, 2016. **18**(19): p. 13216-13222.

37.   Nicholas, J.D. and S.A. Barnett, *Finite-Element Modeling of Idealized Infiltrated Composite Solid Oxide Fuel Cell Cathodes.* Journal of The Electrochemical Society, 2009. **156**(4): p. B458-B464.

38.   Adler, S.B., A.M. Lane, and B.C.H. Steele, *Electrode kinetics of porous mixed-conducting oxygen electrodes.* Journal of The Electrochemical Society, 1996. **143**(11): p. 3554-3564.

39. Tanner, C.W., K.-Z. Fung, and A.V. Virkar, *The effect of porous composite electrode structure on solid oxide fuel cell performance.* Journal of The Electrochemical Society, 1997. **144**(1): p. 10.

40. Nicholas, J.D. and S.A. Barnett, *Validation of the Simple Infiltrated Microstructure Polarization Loss Estimation (SIMPLE) Model Using Single Layer, Nano-Composite Sm0.5Sr0.5CoO3-x-Ce0.9Gd0.1O1.95 Solid Oxide Fuel Cell Cathodes.* Ionic and Mixed Conducting Ceramics 7, 2010. **28**(11): p. 39-58.

41. Hayd, J., U. Guntow, and E. Ivers-Tiffee, *Electrochemical performance of nanoscaled La0.6Sr0.4CoO3-delta as intermediate temperature SOFC cathode.* Ionic and Mixed Conducting Ceramics 7, 2010. **28**(11): p. 3-15.

42. Jensen, S.H., et al., *A method to separate process contributions in impedance spectra by variation of test conditions.* Journal of The Electrochemical Society, 2007. **154**(12): p. B1325-B1330.

43. Fleig, J., *Solid oxide fuel cell cathodes: Polarization mechanisms and modeling of the electrochemical performance.* Annual Review of Materials Research, 2003. **33**: p. 361-382.

44. Nielsen, J. and J. Hjelm, *Impedance of SOFC electrodes: A review and a comprehensive case study on the impedance of LSM:YSZ cathodes.* Electrochimica Acta, 2014. **115**: p. 31-45.

45. Nielsen, J., T. Jacobsen, and M. Wandel, *Impedance of porous IT-SOFC LSCF:CGO composite cathodes.* Electrochimica Acta, 2011. **56**(23): p. 7963-7974.

46. Nielsen, J., T. Klemenso, and P. Blennow, *Detailed impedance characterization of a well performing and durable Ni:CGO infiltrated cermet anode for metal-supported solid oxide fuel cells.* Journal of Power Sources, 2012. **219**: p. 305-316.

47. Utz, A., et al., *Electrochemical Oxidation at SOFC Anodes: Comparison of Patterned Nickel Anodes and Nickel/8YSZ Cermet Anodes.* Solid Oxide Fuel Cells 12 (Sofc Xii), 2011. **35**(1): p. 1669-1682.

48. Chakrave.Bk, *Grain Size Distribution in Thin Films .1. Conservative Systems.* Journal of Physics and Chemistry of Solids, 1967. **28**(12): p. 2401-&.

49. Kungas, R., et al., *Restructuring Porous YSZ by Treatment in Hydrofluoric Acid for Use in SOFC Cathodes.* Journal of the American Ceramic Society, 2011. **94**(7): p. 2220-2224.

50. Hayd, J., et al., *Nanoscaled La0.6Sr0.4CoO3−δ as intermediate temperature solid oxide fuel cell cathode: Microstructure and electrochemical performance.* Journal of Power Sources, 2011. **196**(17): p. 7263-7270.

51. Endler, C., et al., *Oxygen Surface Exchange and Bulk Diffusion Coefficients Evaluated from Porous Mixed Ionic-Electronic Conducting Cathodes.* Ionic and Mixed Conducting Ceramics 7, 2010. **28**(11): p. 71-80.

52. Endler-Schuck, C., et al., *Performance analysis of mixed ionic–electronic conducting cathodes in anode supported cells.* Journal of Power Sources, 2011. **196**(17): p. 7257-7262.

53. Dieterle, L., et al., *Microstructure of Nanoscaled La0.6Sr0.4CoO3-δ Cathodes for Intermediate-Temperature Solid Oxide Fuel Cells.* Advanced Energy Materials, 2011. **1**(2): p. 249-258.

54. Peters, C., A. Weber, and E. Ivers-Tiffee, *Nanoscaled (La(0.5)Sr(0.5))CoO(3-delta) thin film cathodes for SOFC application at 500 degrees C < T < 700 degrees C.* Journal of The Electrochemical Society, 2008. **155**(7): p. B730-B737.

55. Hayd, J. and E. Ivers-Tiffee, *Detailed Electrochemical Study on Nanoscaled La0.6Sr0.4CoO3-delta SOFC Thin-Film Cathodes in Dry, Humid and CO2-Containing Atmospheres.* Journal of The Electrochemical Society, 2013. **160**(11): p. F1197-F1206.

56. Dieterle, L., et al., *Structural and chemical properties of nanocrystalline La0.5Sr0.5CoO3−δ layers on yttria-stabilized zirconia analyzed by transmission electron microscopy.* Journal of Materials Science, 2008. **43**(9): p. 3135-3143.

57. Gao, Z., et al., *A perspective on low-temperature solid oxide fuel cells.* Energy & Environmental Science, 2016. **9**(5): p. 1602-1644.

58. Kilner, J.A. and M. Burriel, *Materials for Intermediate-Temperature Solid-Oxide Fuel Cells.* Annual Review of Materials Research, Vol 44, 2014. **44**: p. 365-393.

59. Wachsman, E.D. and K.T. Lee, *Lowering the Temperature of Solid Oxide Fuel Cells.* Science, 2011. **334**(6058): p. 935-939.

60. Stambouli, A.B. and E. Traversa, *Solid oxide fuel cells (SOFCs): a review of an environmentally clean and efficient source of energy.* Renewable & Sustainable Energy Reviews, 2002. **6**(5): p. 433-455.

61. Laguna-Bercero, M.A., *Recent advances in high temperature electrolysis using solid oxide fuel cells: A review.* Journal of Power Sources, 2012. **203**: p. 4-16.

62. Bierschenk, D.M., J.R. Wilson, and S.A. Barnett, *High efficiency electrical energy storage using a methane-oxygen solid oxide cell.* Energy & Environmental Science, 2011. **4**(3): p. 944-951.

63. Jensen, S.H., et al., *Large-scale electricity storage utilizing reversible solid oxide cells combined with underground storage of CO2 and CH4.* Energy & Environmental Science, 2015. **8**(8): p. 2471-2479.

64. Sundmacher, K., L.K. Rihko-Struckmann, and V. Galvita, *Solid electrolyte membrane reactors: Status and trends.* Catalysis Today, 2005. **104**(2-4): p. 185-199.

65. Bouwmeester, H.J.M., *Dense ceramic membranes for methane conversion.* Catalysis Today, 2003. **82**(1-4): p. 141-150.

66. Dyer, P.N., et al., *Ion transport membrane technology for oxygen separation and syngas production.* Solid State Ionics, 2000. **134**(1-2): p. 21-33.

67. Wang, L., et al., *Oxygen exchange kinetics on solid oxide fuel cell cathode materials-general trends and their mechanistic interpretation.* Journal of Materials Research, 2012. **27**(15): p. 2000-2008.

68. Tarancon, A., et al., *Layered perovskites as promising cathodes for intermediate temperature solid oxide fuel cells.* Journal of Materials Chemistry, 2007. **17**(30): p. 3175-3181.

69. Kilner, J.A., R.A. DeSouza, and I.C. Fullarton, *Surface exchange of oxygen in mixed conducting perovskite oxides.* Solid State Ionics, 1996. **86-8**: p. 703-709.

70. Adler, S.B., *Factors governing oxygen reduction in solid oxide fuel cell cathodes.* Chemical Reviews, 2004. **104**(10): p. 4791-4843.

71. Ratke, L. and P.W. Voorhees, *Growth and coarsening: Ostwald ripening in material processing*. 2002, Berlin, New York: Springer.

72. Hayd, J., et al., *Nanoscaled La0.6Sr0.4CoO3-delta as intermediate temperature solid oxide fuel cell cathode: Microstructure and electrochemical performance.* Journal of Power Sources, 2011. **196**(17): p. 7263-7270.

73. Gong, Y.H., et al., *Atomic Layer Deposition Functionalized Composite SOFC Cathode La0.6Sr0.4Fe0.8Co0.2O3-delta -Gd0.2Ce0.8O1.9: Enhanced Long-Term Stability.* Chemistry of Materials, 2013. **25**(21): p. 4224-4231.

74. Wang, W.S., et al., *The stability of LSF-YSZ electrodes prepared by infiltration.* Journal of The Electrochemical Society, 2007. **154**(5): p. B439-B445.

75.   Sholklapper, T.Z., et al., *Enhancing Cathode Performance and Anode Sulfur/Carbon Tolerance of SOFCs by Nano-Infiltration.* Solid Oxide Fuel Cells 10 (Sofc-X), Pts 1 and 2, 2007. **7**(1): p. 837-843.

76.   Nelson, W., *Accelerated Testing: Statistical Models, Test Plans, and Data Analysis.* 1990, Hoboken, NJ: John Wiley and Sons, Inc.

77.   Jung, W. and H.L. Tuller, *Investigation of surface Sr segregation in model thin film solid oxide fuel cell perovskite electrodes.* Energy & Environmental Science, 2012. **5**(1): p. 5370-5378.

78.   Kubicek, M., et al., *Relationship between Cation Segregation and the Electrochemical Oxygen Reduction Kinetics of La0.6Sr0.4CoO3-delta Thin Film Electrodes.* Journal of The Electrochemical Society, 2011. **158**(6): p. B727-B734.

79.   Druce, J., et al., *Surface termination and subsurface restructuring of perovskite-based solid oxide electrode materials.* Energy & Environmental Science, 2014. **7**(11): p. 3593-3599.

80.   Crumlin, E.J., et al., *Surface strontium enrichment on highly active perovskites for oxygen electrocatalysis in solid oxide fuel cells.* Energy & Environmental Science, 2012. **5**(3): p. 6081-6088.

81.   Gong, Y.H., et al., *Stabilizing Nanostructured Solid Oxide Fuel Cell Cathode with Atomic Layer Deposition.* Nano Letters, 2013. **13**(9): p. 4340-4345.

82.   Harrison, W.A., *Origin of Sr segregation at La1-xSrxMnO3 surfaces.* Physical Review B, 2011. **83**(15).

83.   Oh, D., D. Gostovic, and E.D. Wachsman, *Mechanism of La0.6Sr0.4Co0.2Fe0.8O3 cathode degradation.* Journal of Materials Research, 2012. **27**(15): p. 1992-1999.

84.   la O', G.J., R.F. Savinell, and Y. Shao-Horn, *Activity Enhancement of Dense Strontium-Doped Lanthanum Manganite Thin Films under Cathodic Polarization: A Combined AES and XPS Study.* Journal of The Electrochemical Society, 2009. **156**(6): p. B771-B781.

85.   Decorse, P., G. Caboche, and L.C. Dufour, *A comparative study of the surface and bulk properties of lanthanum-strontium-manganese oxides La1-xSrxMnO3 +/-delta as a function of Sr-content, oxygen potential and temperature.* Solid State Ionics, 1999. **117**(1-2): p. 161-169.

86.   Haider, M.A., A.A. Vance, and S. McIntosh, *Activation of LSM-based SOFC Cathodes - Dependence of Mechanism on Polarization Time.* Solid Oxide Fuel Cells 11 (Sofc-Xi), 2009. **25**(2): p. 2293-2299.

87.   Viswanathan, K., P.V.R. Iyer, and B.P. Mani, *Estimation of Specific Surface-Area and Shape Factors.* Industrial & Engineering Chemistry Process Design and Development, 1982. **21**(2): p. 345-348.

88.   Chakrave.Bk, *Grain Size Distribution in Thin Films .2. Non-Conservative Systems.* Journal of Physics and Chemistry of Solids, 1967. **28**(12): p. 2413-&.

89.   Harris, P.J.F., E.D. Boyes, and J.A. Cairns, *The Sintering of an Alumina-Supported Platinum Catalyst Studied by Transmission Electron-Microscopy.* Journal of Catalysis, 1983. **82**(1): p. 127-146.

90.   McCarty, J.G., et al., *Thermal coarsening of supported palladium combustion catalysts.* Journal of Physical Chemistry B, 2005. **109**(6): p. 2387-2391.

91.   Oksuzomer, M.A.F., et al., *Microstructure and ionic conductivity properties of gadolinia doped ceria (GdxCe1-xO2-x/2) electrolytes for intermediate temperature SOFCs prepared by the polyol method.* Ceramics International, 2013. **39**(7): p. 7305-7315.

92.   Hong, T., Y. Wang, and C.R. Xia, *Nano-structure Effect on Solid State Fuel Cells Cathode Durability.* Journal of Inorganic Materials, 2013. **28**(11): p. 1187-1194.

93.   Burye, T.E. and J.D. Nicholas, *Improving La0.6Sr0.4Co0.8Fe0.2O3-delta infiltrated solid oxide fuel cell cathode performance through precursor solution desiccation.* Journal of Power Sources, 2015. **276**: p. 54-61.

94.   Yu, A.S., et al., *Modification of SOFC Cathodes by Atomic Layer Deposition.* Journal of The Electrochemical Society, 2013. **160**(11): p. F1225-F1231.

95.   Jiang, S.P. and J.G. Love, *Observation of structural change induced by cathodic polarization on (La,Sr)MnO(3) electrodes of solid oxide fuel cells.* Solid State Ionics, 2003. **158**(1-2): p. 45-53.

96.   Wang, W. and S.P. Jiang, *A mechanistic study on the activation process of (La, Sr)MnO3 electrodes of solid oxide fuel cells.* Solid State Ionics, 2006. **177**(15-16): p. 1361-1369.

97.   Kuznecov, M., et al., *Diffusion controlled oxygen transport and stability at the perovskite/electrolyte interface.* Solid State Ionics, 2003. **157**(1-4): p. 371-378.

98.   Yakal-Kremski, K., et al., *Effect of Current Switching on LSM-YSZ Composite Electrode Durability.* Electrochemical Synthesis of Fuels 1, 2012. **41**(33): p. 129-136.

99.   Hughes, G.A., et al., *Durability Testing of Solid Oxide Cell Electrodes with Current Switching.* Journal of The Electrochemical Society, 2012. **159**(12): p. F858-F863.

Appendix A

Supporting Data

7.4   Table A1. Particle sizes for SSC samples of varied infiltration loading

Sample Thickness (µm)	1 µl	1.5 µl	2 µl	Diameter (nm)	Std. dev. (nm)
19.177	4	x	x	86.35	19.21
20.398	x	4	x	79.60	26.06
19.836	x	x	4	40.62	9.69
19.177	4	x	x	86.35	19.21
17.881	4	x	x	75.87	18.24
15.819	4	x	x	77.88	23.14
15.292	4	x	x	61.19	19.36
15.245	4	x	x	78.81	19.96
14.475	4	x	x	40.13	9.48
12.746	4	x	x	39.14	19.36
11.825	4	x	x	27.64	8.90
23.450	2	x	x	68.94	24.10
18.902	2	x	x	66.18	13.64
14.395	2	x	x	62.08	12.45
11.869	2	x	x	68.00	15.64
20.240	x	x	2	52.07	15.49
19.836	x	x	4	40.62	9.69

7.5 Table A2. Model Parameters determined by fitting degradation data for SSC and LSCF cathodes

Sample	SSC	LSCF
E_D (eV)	2.81	2.9
$K_{D,0}$ (cm^2/s)	1.85×10^{-13}	8.98×10^{-13}
R_s at 600°C (Ω cm^2)	25	28.5
L (cm)	0.002	0.002
σ (S/cm)	0.0024	0.003
C	5-7	6
f	0.2-0.25	0.12
$l_{C,0}$ (cm)	5.0×10^{-5}	3.8×10^{-5}